EUMETSAT Satellite Application Facility on

Support to Operational Hydrology and Water Management


# Algorithm Theoretical Baseline Document (ATBD)

# for product H18 – P-IN-ONN-ATMS

## P-IN-ONN-ATMS - Precipitation rate at ground by ATMS-MW cross-track scanner

| | |
|---|---|
| Reference Number: | SAF/HSAF/ATBD-H18 |
| Issue/Revision Index: | 1.0 |
| Last Change: | 12 January 2016 |

## DOCUMENT CHANGE RECORD

| Issue / Revision | Date | Description |
|---|---|---|
| 1.0 | 12/01/2016 | Baseline version prepared for PCR |

**INDEX**

## List of Tables



## List of Figures

# 1 Introduction to product H18

## *1.1 Sensing principle*

The availability of data from the Advanced Technology Microwave Sounder (ATMS), a cross-track scanner radiometer on-board the Suomi National Polar-orbiting Partnership (Suomi NPP) satellite, represents an important step in short and long-term weather forecasting and environmental monitoring. Combining the capabilities of its predecessor sounders such as the Advanced Microwave Sounding Unit-A (AMSU-A) and the Microwave Humidity Sounder (MHS) aboard NOAA-18 and NOAA-19 and the ESA MetOp-A and MetOp-B satellites, ATMS provides sounding observations with improved resolution, sampling and coverage for retrieving atmospheric vertical temperature and humidity profiles. Moreover, this new-generation instrument provides more information about surface, vertical distribution of hydrometeors, precipitation, and other key environmental variables.

With regard to the precipitation it should be mentioned that, although the reliable knowledge of precipitation intensity and accumulation is essential for understanding the global hydrological and energy cycles, precipitation estimate (from satellite and from the surface) is complicated by several factors: the large variability of the precipitation in time and space, the conversion of satellite measurements into quantitative precipitation estimates (an exact quantitative relation between surface rain rate and observed brightness temperatures is nonlinear and difficult to establish due to its complex dependence on the microphysical structure of precipitating clouds), uncertainties associated to rain gauges (and to their spatial distribution), and radar measurements (i.e., attenuation, beam-blocking) and their unavailability in several regions in the world and over ocean (Bennartz and Petty, 2001; Tang et al., 2015; Kirstetter et al., 2012).

The contribution of ATMS in this direction is expected not only in relation to the technological improvements over its predecessor sounders but also as contribution to the Global Precipitation Measurement (GPM) mission. As part of the GPM constellation, ATMS also contributes to the new generation of global precipitation products, providing more accurate instantaneous precipitation estimates thanks to more frequent observations over the globe (3-hourly global coverage between 68° S and 68° N), the use of intercalibrated brightness temperatures from all different PMW radiometers, and the availability of a common, global observatory of 3-D precipitation structure at 5 km resolution (GPM Core Observatory) (Hou et al., 2014).

H18 (also called Passive Microwave Neural-network Precipitation Retrieval algorithm – PNPR v2) algorithm, which is also based on the neural network (NN) approach, represents an evolution of the previous H02A/B (PNPR) algorithm (Sanò et al., 2015) and contains some improvements to take advantage of the increased performance of ATMS with respect to AMSU/MHS.

NNs represent a highly flexible tool alternative to regression and classification techniques, widely applied in an increasing fields of the meteorological research for their capability to approximate complex nonlinear and imperfectly known functions. NNs have been used in precipitation retrieval -

precipitation being one of the most difficult of all atmospheric variables to retrieve - considering the opportunities offered by the ability to learn and generalize of neural networks.

For more information, please refer to the Products User Manual (PUM).

## *1.2 Main operational characteristics*

ATMS is a total power cross-track scanning microwave radiometer on board the Suomi National Polar-orbiting Partnership (NPP) satellite (and JPSS satellites scheduled for early 2017), with a swath of 2600 km, angular span of ±52.77° relative to nadir (Weng et al., 2012; Goldberg et al., 2013; Zou et al. 2014). During each scan the earth is viewed at 96 different angles, with a spatial sampling of 1.11°. ATMS has 22 channels, ranging from 23 to 183 GHz, providing both temperature soundings from the surface to the upper stratosphere (about 1 hPa, ~45 km), and humidity soundings from the surface to upper troposphere (about 200 hPa, ~15 km). Particularly, ATMS channels 1–16 provide measurements at microwave frequencies below 60 GHz in an oxygen absorption band, and channel 17–22 are located at higher microwave frequencies above 89 GHz in a water vapour absorption band at 183.31 GHz. The beam width changes with frequency and is 5.2° for channels 1-2 (23.8-31.4 GHz), 2.2° for channels 3-16 (50.3 - 57.29 GHz and 88.2 GHz), and 1.1° for channels 17-22 (165.5-183.3 GHz). The corresponding nadir resolutions are 74.78 km, 31.64 km and 15.82 km respectively. The outmost FOV sizes are 323.1 km x 141.8 km (cross-track x along-track), 136.7 km x 60.0 km, 68.4 km x 30.0 km, respectively.

Compared with its predecessors AMSU and MHS, ATMS has improved resolution (31.6 km at nadir in the 54 GHz band, vs 48.6 km for AMSU) and sampling (1.11° spatial sampling in the 54 GHz band, vs 3.33° for AMSU) and has the great advantages of a wider swath that practically eliminates the orbital gaps. There are slight differences in the frequencies of ATMS channels 88.2 GHz, 165.5 GHz and 183.31 ± 7.0 GHz with respect to the corresponding MHS channels (89.0 GHz, 157.0 GHz and 190.31 GHz). Three new channels are added compared to AMSU/MHS: channel 4 (51.76 GHz) for lower tropospheric temperature sounding and the two channels 19 and 21 (183.31±4.5 GHz and 183.31±1.8 GHz) to enhance the moisture profiling performance, improving the vertical resolution, and potentially very useful also for precipitation (Surussavadee et al., 2012; Weng et al., 2012; Zou et al., 2014).

## *1.3 Architecture of the products generation chain*

The architecture of the H18 product generation chain is shown in ***Fig. 01***.

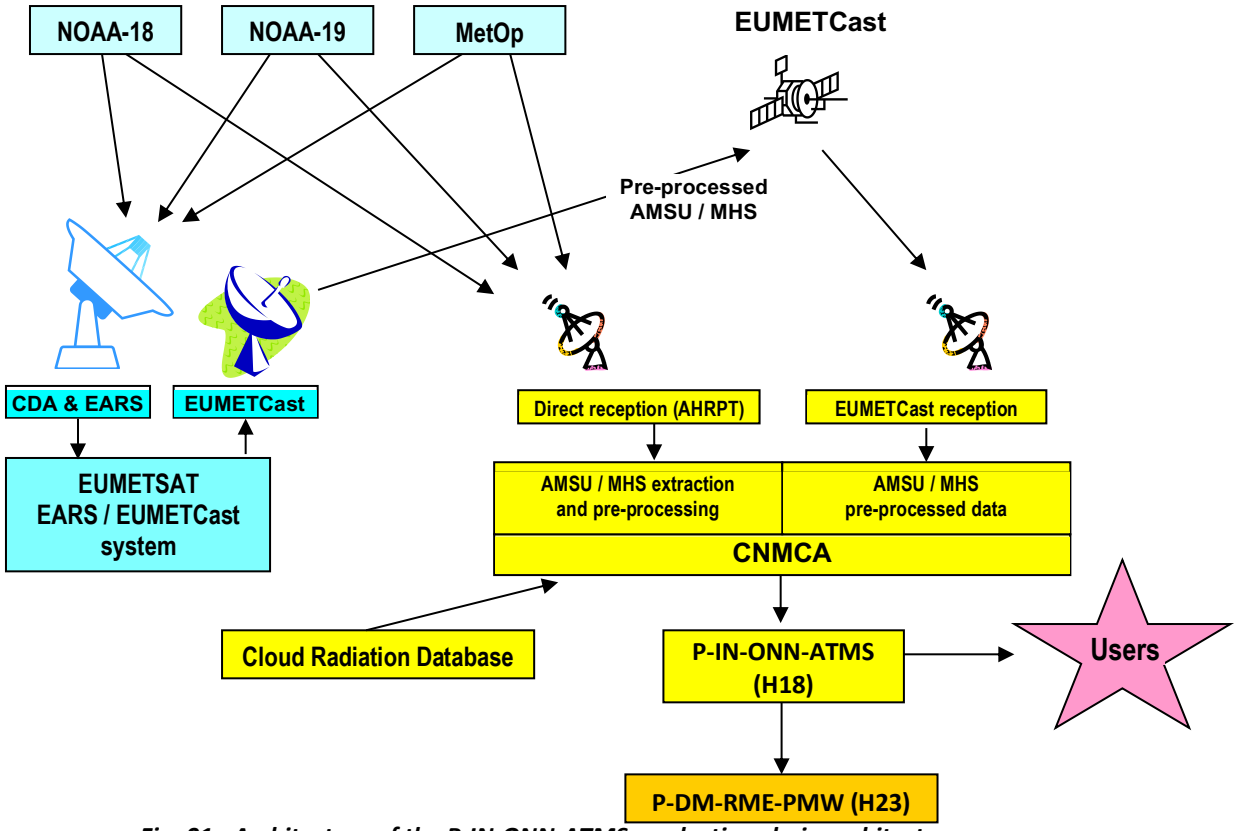


***Fig. 01 - Architecture of the P-IN-ONN-ATMS production chain architecture.***

The P-IN-ONN-ATMS acquisition scheme is based on the EARS/EUMETCast system to cover in near-real-time the areas of interest.

The figure shows that the P-IN-ONN-ATMS product, in addition to be disseminated to the users, is also used to feed the H23 product.

At COMET, the P-IN-ONN-ATMS product is generated on the base of the algorithms and the databases developed and provided by CNR-ISAC.

The product, that includes some online quality control information, is disseminated to the Users by FTP.

## *1.4 Product development team*

Names and coordinates of the main actors for H18 algorithm development and integration are listed in ***Table 01***.

***Table 01 - Development team for product H18***

| | | | |
|---|---|---|---|
| Paolo Sanò (Leader) | CNR Istituto di Scienze dell'Atmosfera e del Clima (ISAC)-UOS Rome | Italy | paolo.sano@artov.isac.cnr.it |
| Daniele Casella | | | daniele.casella@artov.isac.cnr.it |
| Giulia Panegrossi | | | g.panegrossi@isac.cnr.it |
| Stefano Dietrich | | | s.dietrich@isac.cnr.it |

# 2 Processing concept

## *2.1 Basic principles*

H18 (PNPR v2) represents an evolution, for ATMS applications, of previous H02A/B (PNPR) algorithm (Sanò et al., 2015) based on a NN approach, developed at ISAC-CNR for precipitation rate estimation using AMSU/MHS observations. The design procedure of PNPR is described by Sanò et al. 2015; however, some important aspects are reviewed here for completeness.

A significant point in the design of PNPR is the choice of the TB differences in the water vapour absorption band channels at 183 GHz as input to the neural network. Opaque channels around 183.31 GHz were originally designed to retrieve water vapour profiles due to their different sensitivity to specific layers of the atmosphere (Wang et al., 1997; Staelin and Chen, 2000; Blackwell and Chen, 2005). However, these channels have shown great potentials for precipitating cloud characterization and for precipitation retrieval. The different penetration ability of these channels in the atmosphere can be exploited to obtain some criteria for the characterization of precipitation as weak, moderate, strong convection or stratiform (Hong et al., 2005; Burns et al., 1997; Wang et al., 1989, 1997; Funatsu et al., 2007, 2009), using the TB differences Δ17, Δ13, and Δ37 (corresponding respectively to the differences between the 183.31±1 and 183.31±7 GHz, 183.31±1 and 183.31±3 GHz, and 183.31±3 and 183.31±7 GHz channels). The PNPR algorithm for AMSU/MHS has been designed to work over the whole Meteosat Second Generation (MSG) disk area (60°S-75°N, 60°W-60°E) and is based on two distinct NN for European/Mediterranean area and for African area (Panegrossi et al., 2014). In the design of H18, the same criteria used for PNPR were followed, but some changes were needed to take into account the improvements of ATMS with respect to AMSU/MHS. Moreover, another important difference consists in having designed a unique NN capable of operating on the whole MSG disk area.

# 3 Algorithm description

The following Sections describe the algorithms used in the various modules of the precipitation products generation chain. The degree of detail is consistent with the requirement of a manageable document. For further details, please refer to Sanò et al. (2015) for the Neural Network algorithm description and to Panegrossi et al. (2014) for the extension of the algorithm to Africa and Southern Atlantic.

## *3.1 Precipitation screening*

The screening procedure concerns the identification of potentially precipitating pixels. Channels used for this purpose should be sensitive to precipitation but should not exhibit large angle-dependent variations and surface variations.

Over all background surfaces except over desert the screening of not-precipitating pixels is based on the methodology described in Mugnai et al. (2013b). All pixels with brightness temperatures at 183±7 GHz that are below a threshold T7 are flagged as potentially precipitating, where

$T_7 = 0.667\ (T^{max}_{53.6} - 248) + 252 + 6 \cos\theta$

and where $\vartheta$ is the satellite zenith angle and $T^{max}_{53.6}$ is the spatially filtered limb-corrected 53.6 GHz brightness temperature obtained by selecting the warmest brightness temperature within a 7×7 array of ATMS pixels. It has been seen that the threshold $T_7$ can vary with atmospheric temperature. This threshold was determined empirically.

However, the 183±7 GHz channel can become sensitive to surface variations in very cold, dry atmospheric conditions. When $TB_{53.6}$ is less than 248 K, the 183±3 GHz brightness temperature is compared to a threshold $T_3$.

$T_3 = 242.5 + 5 \cos\theta$

In that case, if $TB_{183\pm3}$ is less than $T_3$, the pixel is flagged as potentially precipitating. The thresholds $T_7$ and $T_3$ are slightly colder than a saturated atmosphere would be, implying the presence of a microwave-absorbing or scattering cloud. It is possible for the 183±3 GHz and the 183±1 GHz channels to be sensitive to surface variations. If $TB_{53.6}$ is less than 242 K, then the pixel is assumed not to be precipitating.

Over desert (or arid land) the screening of not-precipitating pixels is based on the methodology developed by Casella et al. (2015). The Arid Land pixels have been identified looking at the mean annual difference of the DMSP SMISS 19 GHz V and H channels (Grody, 1991). Although the presence of clouds may reduce the polarization difference, this effect may be minimized by averaging the TB difference over a long period. One year (2011) of SSMIS observations over the area of interest has been used, selecting the observations over land, and remapping them on a regular grid in latitude and longitude (with 0.5 degree spacing). The difference of the TBs of the 19 GHz V and H channels ($dTB_{19}$) was calculated for each grid point and then averaged over a year. If the mean annual difference of $dTB_{19}$ was higher than 15 K the area corresponding to that grid point was identified as desert or arid land. ***Figure 02*** shows the results of this procedure. It is clear how the Sahara desert and the Arabian desert have been correctly identified as arid land. Smaller areas of arid land also appear in Iran (including the Dasht-e Kavir and the Dasht-e lut deserts) and in the African continent (including the Kalahari desert in South-West Africa and arid regions in the continental Horn of Africa). However some small deserts near to the coast have been not correctly identified, i.e. the Namib Desert in Namibia and the Danakil Desert in the African coast of the Red sea. The Coast pixels have been excluded from this test to eliminate the polarization difference due to the sea surface emissivity.

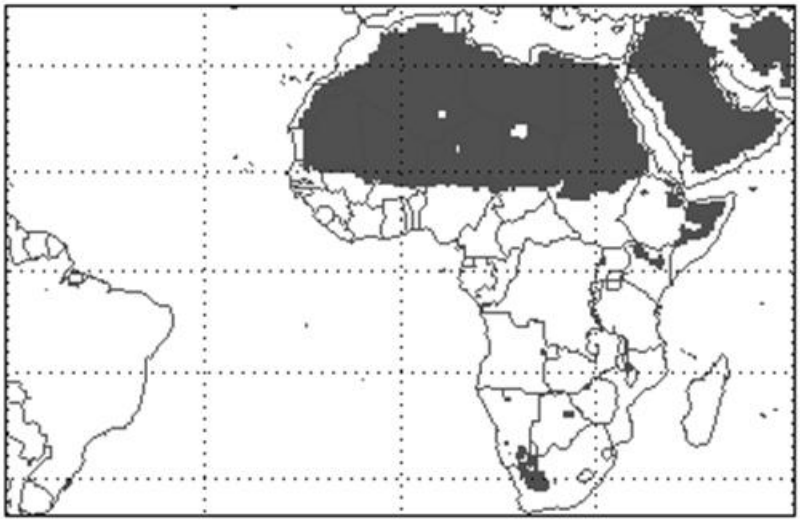

**Figure 02: Map of areas identified as desert or arid land (Casella et al., 2015).**

The screening for the Arid Land pixels is based on a Canonical Correlation Analysis (CCA) approach described in detail by Casella et al. (2015). The CCA approach marks as "rain" those pixels where:

$CV = \sum_{i=1}^{n} a_i \left(TB^i - \overline{TB}_R^i\right) > 2.4\ [K]$

where the index *i* spans over the *n* available channels of the radiometer ATMS, $TB^i$ are the brightness temperatures in each pixel, and $TB_m^i$ are the mean brightness temperatures for each channel computed over a full two-year dataset (2011-2012) used in Casella et al. (2015) where the coefficients $a_i$, and the threshold value equal to 2.4 K have been derived. The coefficients of the CCA analysis ($a_i$) and the values for $TB_m^i$ are provided in Table 02.

***Table 02: List of CCA coefficients and mean TB values used by the precipitation screening algorithm for Arid Land (desert)***

| **ATMS** | | **Arid Land** | |
|---|---|---|---|
| ***Threshold*** | | **2.4 K** | |
| ch. # | ch. Name [GHz] | a | $TB_m$ |
| 1 | 88.2 | 0.07 | 231.00 |
| 2 | 165.5 | -0.05 | 270.72 |
| 3 | 183.3±1 | 0.01 | 245.48 |
| 4 | 183.3±3 | 0.05 | 258.51 |
| 5 | 183.3±7 | -0.08 | 267.58 |
| 6 | 23.8 | -0.05 | 186.65 |
| 7 | 31.4 | 0.20 | 165.92 |
| 8 | 50.3 | -0.29 | 230.79 |
| 9 | 52.8 | 0.13 | 261.44 |
| 10 | 53.6 | -0.11 | 256.34 |
| 11 | 54.4 | 0.02 | 238.66 |
| 12 | 54.9 | 0.17 | 228.55 |
| 13 | 55.5 | -0.08 | 215.23 |

## 3.2 The Precipitation Retrieval Algorithm

### 3.2.1 The neural network approach

The neural network is a highly flexible tool alternative to regression and classification techniques. It allows to approximate unknown complicated non linear functions to an arbitrary degree of accuracy (Hsu et al., 1997; Shi, 2001; Chen et al., 2006; Bellerby, 2007; Marzban, 2009).

***Fig. 03*** shows a feedforward multilayer neural network with ni inputs, n1 nodes in the first (input) layer (nodes are called also perceptrons or neurons), n2 and n3 nodes in the second and third layer (hidden layers) respectively, and one output layer. Each node has its own transfer function. The nodes are connected by links that transfer the weighted output of a node to the linked nodes of the following layer. In this following layer, each node receives, as input to its transfer function, a weighted sum of the outputs of the previous layer. The output of the transfer function corresponds to the output of each node. For example, the output of a node (k-th), $y_k$, of the first hidden layer takes the form:

$$y_k(\omega, x) = f_2\left[\sum_{j=1}^{n1} \omega_{kj} * f_1 * \left(\sum_{t=1}^{ni} \omega_{jt} * x_t + b1\right) + b2\right]$$

where $x_t$ are the input signals (ni values), $\omega_{jt}$ are the weights connecting the inputs to the nodes of the input layer and $\omega_{kj}$ the weights connecting the nodes of the input layer to the nodes of the first hidden layer, f1 and f2 are the transfer functions of the input layer and the first hidden layer, and b1 and b2 are the bias of nodes of the two layers.

The estimation of the weights is performed in the training phase. During this phase a training database is used (providing the network with synthetic input and output data).

In backpropagation network, during the training (Levenberg-Marquardt algorithm), when the network is given an input, the signal propagates forward from the input layer of nodes, through each internal layer, to the output layer. The node in the output layer produces an output ($y_i$), which is compared to the i-th target output ($t_i$) defined in the training set. An error value is calculated as

$$E = \frac{1}{n}\sum_{i=1}^{n}(y_i - t_i)^2$$

where n is the number of elements of the training set. The network corrects its weights to lessen the errors. The correction mechanism starts with the output neuron and propagates backward through each internal layer to the input layer, and modify the value of each weight (i.e. $\omega_{ij}$) in relation to its contribution to the error $\left(\frac{\partial E}{\partial \omega_{ij}}\right)$. The iteration continues in order to minimize the error.

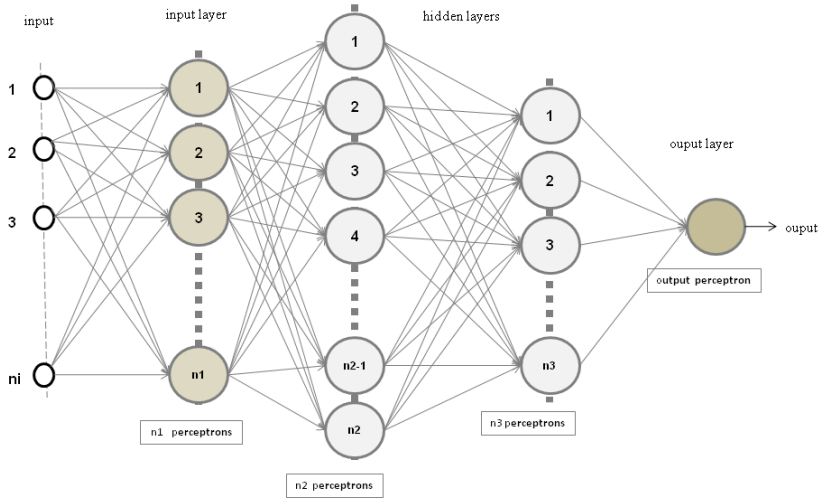


***Fig. 03*** **- Schematic diagram of a multilayer neural network (two hidden layers).**

### *3.2.2 Training the ANN by CRM simulations*

Since the relationship between precipitation and satellite brightness temperatures is nonlinear and imperfectly known, the retrievals here employ neural networks trained with tested physical models.

The training database for the H18 algorithm is based on the same physical foundation used for H01 (PR-OBS-1) (a physically-based Bayesian algorithm, using a Cloud Dynamic Radiation Database (CDRD), see Casella et al., 2013, and Sanò et al., 2013)), and H02A/B (PNPR) (Sanò et al., 2015) -- including the same cloud resolving simulations and RTE modelling methodology -- for calculating simulated satellite TB vectors consistent with the ATMS PMW radiometers' channel frequencies, viewing angles and view-angle dependent IFOV sizes along the scan projections. While the CDRD algorithm uses its database repeatedly to obtain *a priori* potential solution profiles for its Bayesian solver for retrieval situations at the times they occur, the H18 (and H02A/B) algorithm uses its database only once during the training process, to develop the functional relationships needed between the inputs (*i.e.*, radiometer TBs, geographical/seasonal factors, pixel view angle) and the outputs (*i.e.*, surface precipitation rate, phase flag, and quality index).

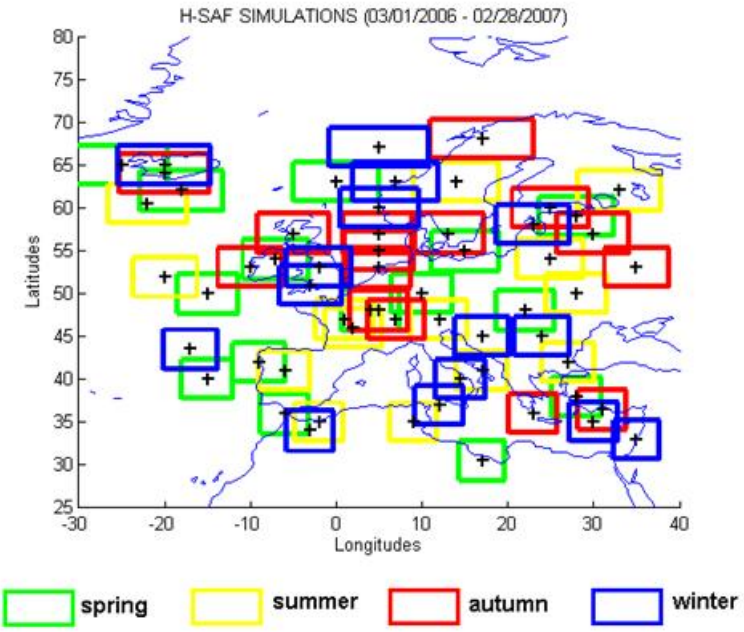


***Fig. 04 - Inner domains of the 60 NMS simulations over the H-SAF area, divided by season***

The dataset for H18 has been expanded to include simulations over Africa and Southern Atlantic. The original dataset used, for the H-SAF area, was made of sixty simulations of different precipitation events over the European area for the period between March 2006 - February 2007 taking into account the various climatic regions, types of precipitation and seasonal variations. ***Fig .04*** shows the inner domains of the 60 simulations. The databases were made 15 simulations for each season, selected in order to have the database as complete as possible.

This dataset has been expanded to include 34 more simulations representative of the climatology and precipitation systems characteristic of Africa and Southern Atlantic (Panegrossi et al., 2014). The events have been selected on the basis of the Tropical Rainfall Measuring Mission (TRMM) Precipitation Radar (PR) observations (in particular the Rain Type flag and the Freezing level height) to select specific events over different climatic regions (shown in ***Fig. 05***) and to cover as much as possible the climatic variability in the area of interest with a limited number of simulations.

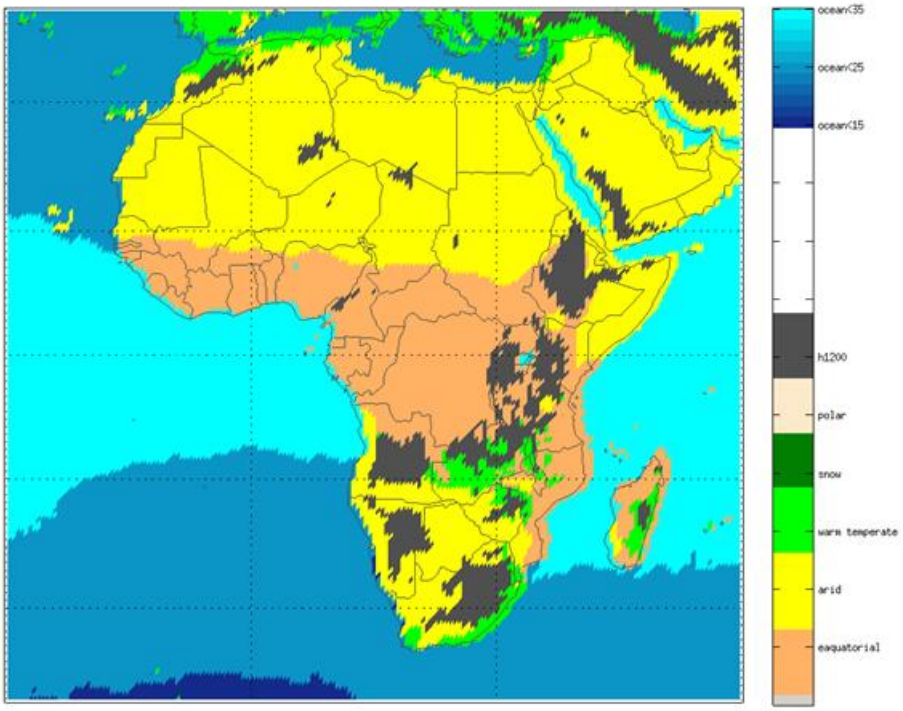


**Fig. 05 – Climatic regions identified over the African continent and represented in the database used in H18**

***Figure 11*** shows and example of a TRMM PR overpass over Africa, with PR derived Rainfall rate, Freezing level height and rain type for one of the simulated events occurred on 02/08/2007. **Table 03** provides the list of all cases selected to generate the database for the African regions, while ***Fig. 07*** shows the map of the spatial distribution of the inner domain of the 34 simulations over Africa.

All simulations have been carried out carried out using the cloud resolving model University of Wisconsin-Non-hydrostatic Modelling System (UW-NMS) (Tripoli, 1992, Tripoli and Smith, 2014).

For each simulation, three two-way nested grids are configured. The vertical grid extends to 17 km divided into 36 levels with variable, height-dependent grid spacing. The horizontal grid configuration is comprised of: (1) an outer domain of 4,500 x 4,500 km at 50-km resolution, (2) a first interior domain of 900 x 900 km at 10-km resolution, and (3) a second interior and innermost domain of 500 x 500 km at 2-km resolution. Simulation cases are selected to ensure thorough sampling over an extensive manifold of multi-channel TBs and across a wide range of meteorological and microphysical conditions containing precipitation.

Each simulation was run for 24 or 36 hours for the European database, and 48 hours for the African database with a 12-hour spin-up time. This initial period is necessary to better initialize the model by adapting the initial data to the maximum resolution of the model. The NOAA National Center for Environmental Prediction (NCEP) Global Forecasting System (GFS) gridded analysis fields at about 100 km resolution were used as initial conditions and to nudge the boundaries of the outer grid every six hours throughout the simulation period. After the first 12 hours, the model extracts hydrometeor profiles over the inner domain C – this is done every hour of the remaining simulation time.

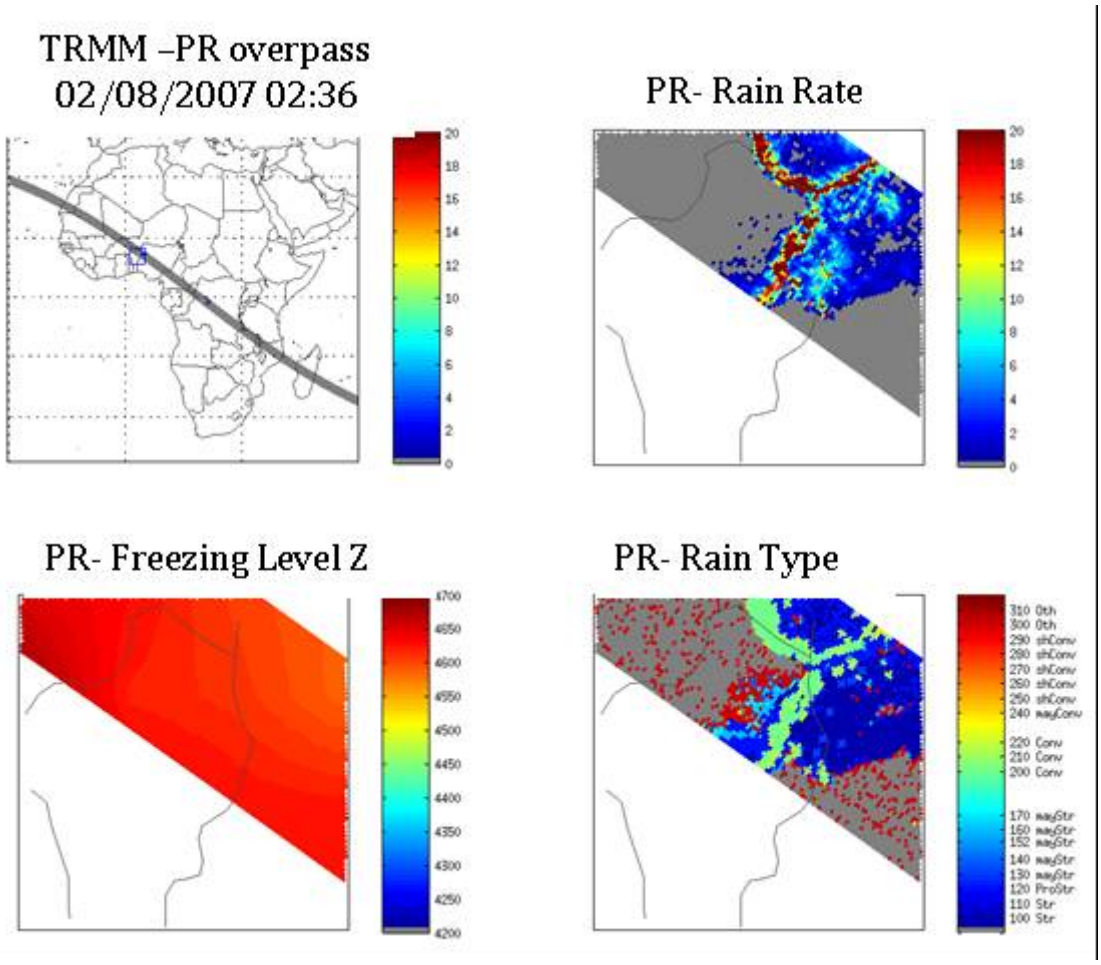


***Figure 06*** **- Example of a TRMM PR overpass over Africa at 02:36 UTC on 02/07/2008 and detail of the area affected by the precipitation with PR derived Rainfall rate (mm/h), Freezing level height (m) and rain type**

***Table 03: List of all simulations used to generate the African database for PR-OBS-2B.***

| # | Event Kind | Climatic Region | Date | UTC time | Lat. | Lon. | NOTE |
|---|---|---|---|---|---|---|---|
| **1** | A | 1 | 20/02/2007 | 00:00 | -25,00 | 42,00 | TrCy Favio (Madagascar) |
| **2** | A | 12 | 21/08/2006 | 00:00 | 8,00 | -15,00 | tropical storm Debby West Africa/Atlantic |
| **3** | A | 4 | 23/07/2006 | 00:00 | 11,00 | 34,50 | floods over Ethiopian highlands |
| **4** | A | 2 | 03/06/2010 | 17:16 | 22,00 | 59,00 | Tropical Cyclone phet (Oman) |
| **5** | B | 1 | 17/07/2008 | 06:21 | 8,81 | 15,83 | Storm over Nigeria-Ciad |
| **6** | B | 2 | 18/06/2006 | 16:52 | 17,00 | 11,80 | scattered precipitation Niger |
| **7** | B | 1 | 02/08/2007 | 02:36 | 10,50 | 3,19 | MCS Benin |
| **8** | B | 1 | 20/09/2007 | 01:33 | 1,50 | 20,14 | MCS NW Congo - fast growing |
| **9** | B | 2 | 03/10/2007 | 20:49 | -21,44 | 26,52 | NE Botswana storm after front |

| | | | | | | | |
|---|---|---|---|---|---|---|---|
| **10** | B | 4 | 07/04/2007 | 14:30 | -22,65 | 45,64 | Madagascar (orographic) |
| **11** | B | 1 | 09/10/2007 | 03:40 | -1,00 | 25,00 | MCS line CONGO |
| **12** | B | 4 | 26/05/2006 | 23:26 | 32,50 | -3,00 | Storm over Atlas |
| **13** | B | 2 | 29/01/2006 | 15:22 | 24,50 | 6,00 | MCS Sahara Algeria |
| **14** | B | 3 | 10/12/2006 | 04:01 | -26,70 | 31,00 | Storm Swaziland |
| **15** | B | 12 | 11/04/2006 | 17:30 | -3,70 | 0,70 | MCS Guinea Gulf |
| **16** | B | 1 | 19/03/2007 | 23:49 | -3,50 | 14,00 | MCS West Central |
| **17** | B | 2 | 15/07/2006 | 19:41 | 14,00 | -8,00 | MCS Sahel |
| **18** | B | 3 | 21/04/2007 | 01:13 | 32,50 | -6,00 | Storm front North Morocco |
| **19** | B | 11 | 20/01/2006 | 17:02 | 32,80 | -24,00 | Storm North Atlantic Ocean |
| **20** | BCDE | 12 | 14/10/2007 | 15:19 | 2,19 | -11,63 | Mixed Guinea Gulf |
| **21** | BD | 1 | 13/05/2006 | 01:01 | 8,61 | 25,50 | Stratiform-Convective South Sudan |
| **22** | BD | 2 | 05/04/2006 | 20:04 | 22,94 | 48,33 | Stratiform-Convective Saudi Arabia |
| **23** | BD | 2 | 05/02/2006 | 22:06 | -26,11 | 22,19 | Stratiform-Convective Botswana |
| **24** | BD | 12 | 18/03/2007 | 01:41 | -11,90 | 12,17 | Stratiform-Convective Angola coast |
| **25** | CE | 11 | 16/11/2007 | 04:20 | -32,65 | -25,08 | Shallow-warm line South Atlantic |
| **26** | CE | 1 | 06/08/2007 | 23:50 | -16,25 | 49,99 | Shallow-warm Madagascar |
| **27** | CE | 2 | 29/01/2006 | 05:41 | 16,98 | 39,43 | Shallow-warm Red Sea |
| **28** | CE | 2 | 10/05/2007 | 03:27 | -34,90 | 20,35 | Shallow-warm line South Africa |
| **29** | D | 2 | 16/02/2006 | 23:18 | 18,49 | -5,36 | Stratiform Sahara Mauritania |
| **30** | D | 2 | 30/03/2007 | 13:35 | 31,52 | 21,85 | Stratiform Libya NE |
| **31** | D | 6 | 16/12/2006 | 23:07 | -12,70 | 25,96 | Stratiform round Zambia |
| **32** | D | 1 | 29/01/2007 | 00:20 | -10,55 | 37,44 | Stratiform Tanzania |
| **33** | D | 6 | 25/10/2006 | 22:09 | 8,65 | 43,62 | Stratiform Ethiopian Highlands |
| **34** | D | 12 | 22/09/2006 | 15:05 | -2,10 | 59,49 | Stratiform intense N-Indian Sea |

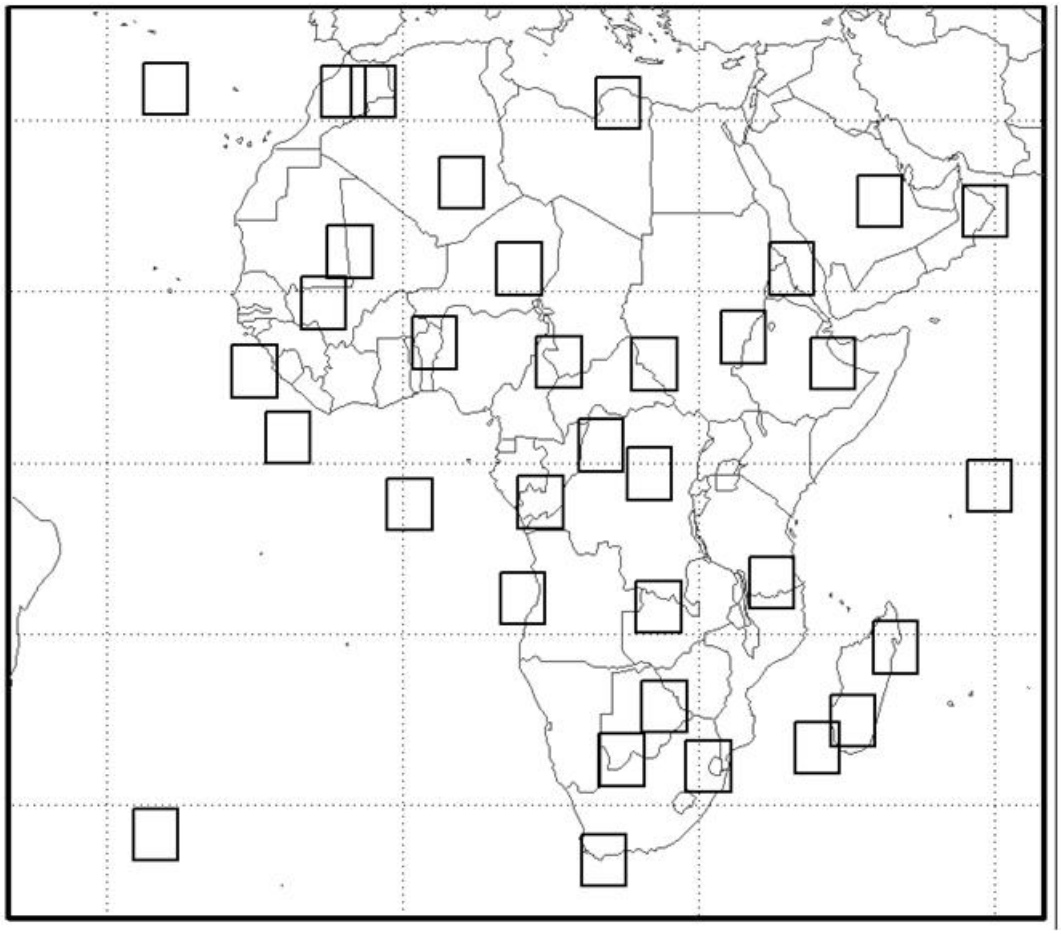

***Fig. 07 – Spatial distribution of the Inner domain of the 34 NMS simulations over the African region for the H18 training database***

### *3.2.3 The UW-NMS Cloud Resolving Model*

The UW-NMS model represents the further development of the regional atmospheric modelling system maintained at Colorado State University (see Tripoli and Cotton 1981, 1982, 1986; Cotton et al. 1982, 1986; Tripoli 1992 a,b) with more recent major improvements concerning the model's dynamical conservation properties and its unique variable step topography (VST) surface coordinate system described by Tripoli and Smith (2014). The NMS is a 3-dimensional, non-hydrostatic, nested, scalable regional-mesoscale, prognostic model. It is able to simulate atmospheric phenomena across all relevant scales from microscale, up through mesoscale and out to the synoptic/regional scales. This model is chosen because of its ability to achieve accuracy in simulating scale-interaction processes through imposition of conservation on mass, energy, momentum, vorticity and enstrophy throughout model integration. The underlying model framework uses quasi-compressible closure formulated on an Arakawa "C" grid cast on multiple-nest rotated spherical grids using multiple two-way nesting. The model employs non-Boussinesq dynamics, two-way grid nesting exchanges, and a unique terrain-following VST vertical coordinate system at its lower boundary. The two-way interactive nesting scheme allows increased resolution in focused areas. VST coordinates are able to capture the dynamical consequences of either steep inclinations or subtly varying terrain features without sacrificing accuracy for any type of terrain-induced slope flows at any scale as shown in Tripoli and Smith (2014). A variable ice-liquid water potential temperature is used as the predictive

thermodynamic variable in the model (Tripoli and Cotton 1981). The advantage in using this quantity is its conserved properties for all phase changes. In so doing, potential temperature, water vapour and cloud water are all treated as diagnostic variables.

The UW-NMS microphysical module used for this study is a modified form of the scheme described by Flatau et al. 1989 and Cotton et al. 1986, and more recently improved by Panegrossi (2004). Specifically, in UW-NMS the treatment of ice categories and specifics of the precipitation physics tendencies has been modified from the original published works to enhance their performance. The microphysics is a bulk microphysics parameterization, which includes six hydrometeor categories labelled as: suspended cloud droplets, precipitating rain drops, suspended pristine ice crystals, and precipitating low-density graupel particles (or snow pellets), ice aggregates and high-density graupel particles. Depending on the application, all or some of these categories may be selected. Any combination of frozen and liquid hydrometeors can coexist within the same grid volume at any given time to allow hydrometeor category interaction to take place.

A negative exponential size distribution *N(D)* is assumed for all categories (except cloud droplets and pristine crystals, which are considered monodispersed), and it is given by:

$$N(D) = N_0 e^{-\lambda D}$$

where $N_0$ is the intercept and $\lambda$ is the slope of the distribution. The total concentration of hydrometeors in the distribution can be found by an integration of the distribution:

$$N_t = \int_0^\infty N(D)dD = N_0 / \lambda$$

The mean diameter and the liquid water content are quantities frequently used in cloud modelling applications. The mean diameter $D_m$ is the first moment of the distribution, and it is defined as:

$$D_m = \frac{\int_0^\infty DN(D)dD}{\int_0^\infty N(D)dD}$$

For a negative exponential it becomes:

$$D_m = \frac{1}{\lambda}$$

The liquid water content or ice water content is proportional to the third moment of the distribution:

$$l_h = \int_0^\infty m(D)N(D)dD$$

where *m(D)* is the mass of particles of diameter D. For spherical particles of density $\rho_h$ with negative-exponential size distribution, it becomes:

$$l_h = \pi N_t D^3 m \rho_h$$

An alternative to the liquid water content to describe the mass content of hydrometeors within the cloud is the mixing ratio defined as:

$$r_h = \frac{l_h}{\rho_0}$$

where $\rho_0$ is the dry air density. It is always predicted in UW-NMS, and it is related to the size distribution parameters by:

$$\lambda = \left[ \frac{\pi \rho_h N_t}{\rho_0 r_h} \right]^{\frac{1}{3}}$$

One can see that the distribution can be completely described by assigning a value of either the slope, or the intercept, or the concentration. The model always predicts the total mixing ratio of all condensate (liquid and ice), water vapour mixing ratio, and the mixing ratio of each hydrometeor category, except for cloud droplets whose mixing ratio is diagnosed.

For each hydrometeor category, the UW-NMS model offers the possibility to specify the value either for the slope, or for the intercept, or for the total number concentration. A different method for parameterising each hydrometeor category can be selected where the total concentration (number of particles per unit mass) can be predicted. This option allows the parameters of the size distribution $\lambda$ and $N_0$ to be diagnosed from the mixing ratio and the total concentration, obtaining different values of the slope and the intercept at each grid volume. Mixed-phase particles (i.e. melting graupel) are not included but any combination of liquid and frozen particles is allowed to occur at a given grid point.

For the aim of this project it is very important to describe the parameterization of each hydrometeor category, explaining the major assumptions in the conversion process between one category and the other, and to describe the parameterization of their microphysical properties. Particular emphasis will be given below to the size distribution and density (for the frozen hydrometeors) parameterization, because these are the parameters that directly determine the optical properties

***A - Cloud droplets -*** The cloud water drops are assumed to be of constant size except with respect to the formulations for autoconversion and ice splintering where they are cast in the form of a modified Gamma distribution (Tripoli and Cotton 1981). Their mixing ratio is diagnosed, while their concentration is specified *a priori* since cloud water nucleation is not explicitly considered in the model. The typical characteristic diameter ($D_C$) of cloud droplets is 0.02 mm with the density of pure water ($\rho_w$), *i.e.*, 1 g cm$^{-2}$. Besides the implicit diffusional growth and decay of cloud water due to production of supersaturation built into a diagnostic system, cloud water may be converted to any of the other hydrometeor categories through collection, phoretic contact freezing, or autoconversion directly to rain. Stochastic broadening is parameterized to be dependent on the average cloud-droplet size.

***B - Rain drops –*** For this study, the rain water category is assumed to be distributed in a Marshall-Palmer distribution of specified constant intercept of 0.08 cm$^{-4}$. Rain droplets arise primarily through the collision-coalescence process (warm rain) and the melting of precipitating ice particles (cold rain). In warm-based clouds, like those typical of summertime Alabama or tropical cyclone, both processes are important. Rain droplets are lost to the system primarily through conversion to ice categories (droplet freezing and riming) or evaporation and through loss due to precipitation.

***C - Pristine ice crystals -*** The original pristine ice category of the Flatau parameterization (Flatau et al. 1989) is divided into a snow and pristine category. The original version grouped both nucleated and new crystals together. Since a constant size distribution had been assumed, massive nucleation at cold temperatures would drastically alter the average crystal size and would remove all memory of the growth that some of the larger crystals had been through. Here, riming growth processes are assumed to convert

pristine crystals at their predicted mass to a snow category which represents rimed crystals. Hence, new and mature populations of crystals continue to exist as pristine crystals where massive nucleation occurs, whereas crystals that have substantially increased in mass through riming are separated out in can evolve independently. This was especially important for the simulations of cirrus anvils where influxes of pristine crystals would dominate the old inclusive pristine category sometimes preventing the precipitation of the rimed particles. Both their concentration and mixing ratio are predicted, therefore their mass and size change at each grid point, with a typical $D_C$ of ~0.24 mm. The density ($\rho_p$) is derived according to Flatau et al. (1989), starting with a mass - diameter (*m* - *D*) relationship:

$$D = \beta \left( \frac{m}{K} \right)^{\alpha}$$

where $\alpha$ is a non-dimensional exponential factor, $\beta$ is a size scale factor (in cm) and *K* is a mass normalization factor (in g). For an equivalent volume sphere, the density becomes:

$$\rho_p = \frac{6}{\pi} K \beta^{\alpha} D^{1/\alpha - 3}$$

The three parameters, $\alpha$ *(=0.5)*, $\beta$ (=19.2 cm) and *K (=1g)* depend on the crystal mass in such a manner that as the mass (or size) increases, the density decreases (see Casella et al., 2013 and Smith et al., 2013 for further details). The only source of new crystals are primary and secondary nucleation including sorption and deposition, contact nucleation and splintering. Pristine crystals can be lost through conversion to hard graupel resulting from collection directly onto the graupel surface or through contact freezing of rain droplets, by conversion to soft graupel through the riming of cloud droplets or the conversion to aggregates through the aggregation process. Because pristine ice crystals tend to remain quite small in mass, they can be assumed to melt instantaneously when the temperature of the air exceeds freezing.

***D - Ice aggregates / Snowflakes -*** The aggregate category consists of aggregated crystals formed by collisions among pristine crystals, or pristine crystals other aggregates. Aggregates are assumed to be in a Marshall-Palmer distribution of constant assumed slope, with mean radius of 1650 μm. The implicit assumption is that break-up balances formation. Additional growth is possible from riming and deposition, although strong riming will result in conversion to graupel at a specified rate. Aggregates represent the major source of graupel embryos. Aggregates are lost to melting, evaporation, precipitation fallout processes and conversion to snow pellets through riming processes. For aggregates the size dependent density $\rho_{s/a}$ is given the above equations, where $\alpha$ = 0.419 and $\beta$ = 8.89 cm. The resultant expression is $\rho_a$ *(*$D_C$*)* = 0.015 / [$D_C^{0.6}$] g cm$^{-3}$ (Panegrossi et al., 1998)

***E - Soft graupel / Snow pellets -*** The snow pellets (or soft graupel) category is assumed to follow a Marshall-Palmer distribution with constant intercept of 0.014 cm$^{-4}$. The snow pellets are assumed to grow from their initiation size through vapor-deposition processes and riming of both rain and cloud droplets. There is an assumed conversion formula to convert the soft graupel to the hard graupel category, which is dependent on the riming rate by rain droplets compared to growth rates by other processes and the relative size of collected rain droplets compared to the snow particle size.

Snow represents soft, low-density ice forming when pristine crystals or aggregates become heavily rimed, with their density ($\rho_s$) formulated according to Macklin (1962):

$$\rho_s = \left( -\frac{\hat{r}\hat{U}_{imp}}{T_s} \right)^{b}$$

in which $T_S$ is the surface temperature of the ice substrates (in $^oC$), $\hat{r}$ is a weighted averaged radius (in $\mu m$) and $U_{imp}$ is the weighted average impact velocity of cloud droplets and rain drops (in $m\ s^{-1}$). The values for the *a* and *b* coefficients are 0.23 g $cm^{-3}$ and 0.44, respectively, as reported by Prodi *et al.* (1991). The $\hat{r}$ is calculated by averaging the radii of the cloud droplet and rain drop diameters, weighted by their respective mixing ratios. The $\hat{U}_{imp}$is calculated by averaging the impact velocity between rain drops and snow (*i.e.*, the difference between the terminal velocities of rain drops and snow) with the impact velocity between cloud droplets and snow (*i.e.*, approximately the terminal velocity of snow alone), again weighted by the mixing ratios of cloud droplets and rain drops. The resultant snow density typically covers a range of values from 0.05 - 0.9 g $cm^{-3}$.

***F - Hard graupel / Hailstones -*** The hard graupel category is also assumed to be in a constant intercept (0.071 $cm^{-4}$) Marshall-Palmer distribution and constant density $\rho$ = 0.9 g/$cm^3$. Hard graupel grows or decays from vapor deposition, riming, and melting and conversion from rain, pristine crystals, aggregates and soft graupel categories. Wet growth or dry growth are both modeled and depend on the diagnosed equilibrium temperature of the graupel surface. This temperature depends of the energy balance at the surface of the droplet resulting from conduction with the air versus latent heating or cooling due to evaporation or sublimation onto the particle, and freezing of collected liquid water. At sub freezing, air temperatures, the energy balance determines the proportion of any collected liquid water that can be frozen, given the rate that the particle can conduct heat away to the air. Any excess water that cannot freeze is assumed to be shed as rain. Hence wet or dry growth or melting is modeled at below or above freezing temperatures dependent on the diagnosed energy balance. The results of this balance can be made available for radiative transfer calculations since the existence of a liquid coating dramatically alters radiative properties of the graupel particle.

### *3.2.4 The Radiative Transfer Model*

ATMS radiances were simulated by using a one-dimensional plane-parallel Eddington approximation to the inelastic, steady-state RTE (see Liou, 2002]). The plane-parallel Eddington approximation is well known and widely used especially because of its computational efficiency. It is important to recognize that for the most part, the mean PMW TB differences between a one-dimensional RTE model and fully three-dimensional RTE model (either through use of an analytical approximation scheme or a generalized Monte Carlo method) are within a few degrees in magnitude (see Roberti et al., 1994, Smith et al, 2002) even considering the use of the higher SSMIS frequencies (see Bauer et al., 2006). Although these differences may become significant locally in case of strong horizontal gradients within the cloud microphysical properties such as near cloud edges (*e.g.*, Liu et al., 1996), we have found in our own calculations that the treatment of the optical properties of the ambient hydrometeors and their concomitant treatment in a single scatter framework is far more important in reconciling RTE model calculations with satellite observations, than the particular choice of the core RTE model solution. The last argument is in accordance with the recent study of Kulie et al. (2010) based on several ice scattering models compared within the framework of both passive and active microwave models.

Namely, every vertical profile generated by the model at high resolution is used to generate a plane-parallel precipitating environment, to which the RTM is then applied to compute the upwelling TBs at the different incident viewing angles of the radiometers. The required inputs to the RTM are: suitable temperature / moisture profiles and temperature / emissivity of the surface, as well as vertical profiles of liquid/ice water contents (LWC/IWC) of the various hydrometeors - along with their single-scattering

properties. Surface temperature and vertical profiles are provided by the UW-NMS simulation. Absorption by atmospheric gases at microwave frequencies are calculated according to the Liebe and Gimmestad (1978) and Liebe (1985) clear-moist air refractivity model that provides a combined water vapour – oxygen volume absorption coefficient.

The same 9-member surface emissivity module (SEM) developed and used for the CDRD (PR-OBS-1) algorithm has been used to generate the training database for PR-OBS-2B. For a rough ocean (*i.e.*, an ocean surface undergoing above-surface winds) the SEM employs the ocean emissivity model of English and Hewison (1998); see also Schluessel and Luthardt (1991) and Hewison and English (2000).

This scheme calculates accurate estimates of open sea emissivity between 10 and 200 GHz for observation angles up to 60 degrees and winds between 0 and 20 m $s^{-1}$. For non-frozen land emissivities, we have adopted two different surface emissivity models from Hewison (2001), specifically models for "other forestry" and "bare soil", which we refer to as "vegetated land cover" and "non-frozen bare soil", respectively. For frozen surfaces we have adopted six surface emissivity models from Hewison and English (1999) consisting of "frozen bare soil", "snow-covered forest", "first year ice", "compact snow", "fresh wet snow", and "deep dry snow" -- noting we have imposed various minor name changes from the originals for the frozen surface cases. We also note that the latter four frozen surfaces may be applied to either ocean or land areas. For desert areas (arid land) the model uses the TELSEM emissivity atlas (see Prigent et al., 2006).

For calculations of the single scattering properties of hydrometeors, various assumptions concerning hydrometeor shape are made, since shape information is not comprehensively provided from the NMS bulk microphysical parameterization scheme. In NMS, cloud droplets and rain drops are considered to be spherical and homogeneous, thus their scattering properties can be calculated based on Mie theory. Graupel hydrometeors are assumed to be spherical and homogeneous with a bulk density (mass / volume of a circumscribing sphere) equal to $\rho_g$ (0.9 g/$cm^3$). Thus Mie theory can also be used to calculate graupel optical properties using the index of refraction of a homogeneous mixture of air and ice, according to the average dielectric function of Maxwell-Garnett [36].

In NMS, pristine crystals represent recently formed particles and are assumed to have a hexagonal plate habit, and size / density formulations described in Section 2.1. Alternatively, the RMS represents pristine crystals as many different simple ice crystal shapes, from needles to plates, all assumed to have the same $D_C$ of 0.024 cm which results in an associated density of 0.1 g $cm^{-3}$. In order to calculate their optical properties, the Grenfell and Warren (1999) approximation scheme is used. In this approximation, the single-scattering properties of each non-spherical particle are calculated by means of a collection (concentration) of solid ice spheres $n_S$, all equal in size to one another, with a new equivalent diameter ($D_S$) determined by the ratio of volume over cross-section area ($V$ / $A_{cs}$) of the original particle. The $V$ factor is derived from the NMS. To obtain the $A_{cs}$ factor, the following relationship from [39] is used:

$$A_{cs} / (\pi D_c^2/4) = K_0 D_c^k$$

for various shapes of ice particles. For our calculations, $K_0$ and $k$ are taken as 0.18 $cm^{-1}$ and 0.2707, respectively, as indicated by the aforementioned authors for continental cirrus with mixed habit (noting the circumscribing sphere characteristic diameter $D_C$ must be expressed in cm). The result is that the $D_S$ and $n_S$ of the equivalent spheres are given by:

$$D_s = \frac{\rho_p}{\rho_i} \frac{D_c}{K_0 D_c^k}$$

$$n_s = \left(\frac{K_0}{1-k}\right)\left(\frac{D_c^{3+k}}{K_0 D_s^3}\right)$$

In the NMS, snow and aggregates are porous, low-density and assumed to have variable - complex shapes. In order to represent snow and aggregates as non-spherical particles, we adopt the approximations developed by Surussavadee (2006), Surussavadee and Staelin (2006, 2008a,b) in which the results of several single scattering simulations of non-spherical particles have been reproduced synthetically using the Mie solution for spheres of equivalent mass and a density formulation $\rho(\nu)$ that is a function of frequency ($\nu$). In this fashion, both radii and densities of the simulated hydrometeors are changed to take into account the optical effect of non-sphericity, without altering their masses. In detail, snow and aggregates are approximated by equal-mass spheres that are mixtures of ice and air having densities $0 < \rho(\nu) < 0.9$ g cm$^{-3}$ that depend on habit and $\nu$. It is important to note that $\rho(\nu)$ is that of an optically-equivalent particle and can be quite different from the density of hard ice, as well as different from the bulk density of the original particle itself. The formulation is:

$$\rho(\nu) = \gamma \cdot 10^{-3} \cdot \nu + \eta$$

where for snow (corresponding to plates), the parameters $\gamma$ and $\eta$ are 0.815 g cm$^{-3}$ s$^{-1}$ and 0.012 g cm$^{-3}$, respectively, while for aggregates (corresponding to 6-arm bullet rosettes) they are 0.863 g cm$^{-3}$ s$^{-1}$ and 0.115 g cm$^{-3}$, respectively and $\nu$ is expressed in GHz.

Once individual absorption, scattering, and asymmetry factors have been calculated for the components hydrometeors of a vertical grid cell, they are integrated over the PSDs to obtain bulk absorption / scattering efficiencies and asymmetry factors for the entire microphysical mixture. This process then continues throughout the vertical extent of the microphysical profile. Next, the boundary emissivities (reflectances) from the surface are obtained from the SEM (see next sub-section). Finally, the multiple scattering RTE model is invoked to obtain the simulated TOA satellite TBs. Because Mie equations are used in calculating the scattering phase functions of equivalent spheres, the RMS's RTE model cannot introduce polarization to the radiation field due to the cloud hydrometeors themselves. However, polarization is introduced through the polarized reflecting surface backgrounds.

### *3.2.5 The Instrument model*

In order to mitigate against non-homogeneous IFOV beam filling affecting the retrievals (*i.e.*, variability in precipitation cover within a given IFOV produces errors in retrievals because of the underlying non-linear relationship between TBs and precipitation rates), an effect referred to as non-uniform beam filling (NUBF) error. This is a critical issue for lower frequency / larger IFOV footprints and/or IFOVs situated at scan edges. To reduce NUBF errors, the initial simulated TBs for the database, initially taken at the CRM's 2-km resolution, are spatially averaged (convolved) using the ATMS Gaussian antenna pattern functions out to ±1σ widths, these functions varying with channel frequency and view angle. In replicating the characteristics of the ATMS radiometer, the RMS makes calculations at 45 beam centers ($\vartheta$s) using steps of 1.1° (ignoring the last three pixels at the edge of the scan, due to their low spatial resolution), equivalent to the number of mechanical scan stops used on the ATMS instrument, scanning to either side of nadir over a tilt angle from nadir beam center to edge beam center of 48.33º for a ½ scan angular view field of 49.5º. Therefore, each possible NMS cloud structure must be associated to 45 different TB vectors (for each of the 45 view angles), noting a complete ATMS instrument scan involves 91 steps, but with angular symmetry around the center step.

In the H18 database, the correspondence between TB vectors, along with their associated surface precipitation rates, is complicated by the dependence of spatial resolution along a radiometer scan due to the varying view angle. A variable sensor resolution (VSR) is defined according to the nominal nadir resolution of ATMS, varying from 16 x 16 km$^2$ / circular at nadir to 30 x 68 km$^2$ / ovate at scan edge corresponding to the 45-th ATMS instrument scan. Thus, the surface precipitation rates must be averaged for 45 VSRs with precipitation products delivered to the H-SAF product data centre tagged accordingly. This means that the H18 database is 45 times greater density in precipitation structure entries than the CDRD database.

### *3.2.6 The neural network*

The first objective in the new NN design was the selection of the inputs based on the evaluation of their impact on the performance of the NN or on their sensitivity to precipitation. Consistently with PNPR design and on the basis of the results obtained for AMSU/MHS (Sanò et al., 2015), for the new NN we have initially imposed the use of the three inputs Δ17, Δ13, and Δ37 (Hong et al., 2005; Funatsu et al., 2007, 2009). These TB differences have been proven to be very effective in detecting precipitation, differentiating between different precipitation structures and in the retrieval of rainfall rate. Moreover, an extensive and exhaustive analysis to evaluate the effect of additional inputs on the performance of the NN was carried out. All possible TB differences including the two new ATMS 183 GHz (183.31±1.8 and 183.31±4.5 GHz) channels were considered, and the analysis was based on cross-validation method (CV) (Anders and Korn, 1999; Marzban, 2009), already used for PNPR (Sanò et al., 2015). This method consists, essentially, in comparing the quality of two NNs by evaluating their mean squared prediction error (MSPE) when they are applied to an equal number (M) of validation data sets,

$$\mathrm{CV} = \frac{1}{\mathrm{M}} \sum_{\mathrm{m}=1}^{\mathrm{M}} \mathrm{MSPE}_{\mathrm{m}}.$$

In a first test, only the three differences Δ14, Δ24, and Δ27 (corresponding respectively to the differences between the 183.31±1 and 183.31±4.5 GHz, 183.31±1.8 and 183.31±4.5 GHz, and 183.31±1.8 and 183.31±7 GHz channels) showed a real improvement in the performance. The use of the differences between contiguous channels resulted in fact irrelevant. The subsequent tests with these three new inputs proved that of Δ24, added to Δ17, Δ13, and Δ37, was the input with most significant impact on the performance, and, also to reduce the complexity of the network, only this TB difference was selected as additional input to the NN. Minimize the number of inputs of the NN is, in fact, a key aspect in the algorithm design. Table 04 shows some results obtained during the test.

In the table the various possible differences considered as input to the NN in this analysis are shown in the first column; ΔF = Δ13, Δ37, Δ17 denotes the three difference combination used in the PNPR algorithm. In the second and fourth columns the values of the correlation coefficients between output and target during the learning (RL) phase, and the mean values during the verification (RCV) phase are shown. In the third and the fifth columns the values of the mean squared error during the learning phase (MSEL), and the mean MSPE values during the verification phase (CV) are provided. It is evident in the table that the use of the only new input Δ24 represents the best compromise between the achievement of a good performance and the complexity of the NN. Therefore, Δ24 was selected as additional input to the NN.

Table 04 - Results of the tests for the selection of the inputs to the NN (ΔF = Δ13, Δ37, Δ17)

| INPUT | $R_L$ | $MSE_L$ | $R_{CV}$ | CV |
|---|---|---|---|---|
| **$\Delta_F$** | **0.85** | **0.39** | **0.76** | **0.42** |
| $\Delta_F$ and $\Delta_{14}$, $\Delta_{24}$, $\Delta_{27}$ | 0.78 | 0.64 | 0.70 | 0.68 |
| $\Delta_F$ and $\Delta_{14}$, $\Delta_{24}$ | 0.89 | 0.37 | 0.80 | 0.42 |
| $\Delta_F$ and $\Delta_{14}$, $\Delta_{27}$ | 0.83 | 0.49 | 0.78 | 0.53 |
| $\Delta_F$ and $\Delta_{24}$, $\Delta_{27}$ | 0.81 | 0.50 | 0.70 | 0.54 |
| $\Delta_F$ and $\Delta_{14}$ | 0.87 | 0.37 | 0.79 | 0.41 |
| **$\Delta_F$ and $\Delta_{24}$** | **0.92** | **0.32** | **0.87** | **0.35** |
| $\Delta_F$ and $\Delta_{27}$ | 0.83 | 0.48 | 0.68 | 0.52 |

Another difference, between PNPR v2 and PNPR algorithms is the linear combination of TBs of selected channels, found using canonical correlation analysis (CCA) (applied to the training database) and best correlated with surface precipitation rate, used as additional input to the network (see Sanò et al., 2015). The resulting linear combination for ATMS is composed of the window channels 31.4, 88.2, and 165.5 GHz having the highest correlation coefficients in the CCA analysis in the database (with respect to the surface rain rate) for all types of background surfaces.

With regard to other inputs to the network, in PNPR v2 the same ancillary data used in PNPR were maintained (surface height, the background surface type, season, and the secant of the zenith angle along the ATMS cross-track scan). An additional auxiliary input was added to drive NN in the transition between the European and African area, i.e., the monthly mean total precipitable water (TPW) obtained from ECMWF reanalysis in the 2011-2014 period. It should be mentioned that the use of geographical and environmental/meteorological parameters (including TPW) in PMW precipitation retrieval is essential to reduce the ambiguity intrinsic to the PMW precipitation retrieval process and widely applied in the most advanced retrieval algorithms (for example the NASA GPM Bayesian algorithms [Kummerow et al., 2015, Kidd et al., 2016]).

During the phase of network design and the training process, more than 400 architectures have been tested and an optimal NN has been obtained, where “optimal” refers to the one with best performance, i.e., minimum CV, over the full dynamic range of the inputs, absence of overfitting, and absence of anomalous inhomogeneities in the retrievals (Sanò et al., 2015; Staelin and Surussavadee, 2007).

In summary, ten input variables are used in the NN for ATMS:

1. a linear combination of TBs (LCT) at 31.4, 88.2 and 165.5 GHz obtained from the CCA applied to the training database;

2. Δ17 difference between the TBs of channels 183.31±1 and 183.31±7 GHz;

3. Δ37 difference between the TBs of channels 183.31±3 and 183.31±7 GHz;

4. Δ13 difference between the TBs of channels 183.31±1 and 183.31±3 GHz;

5. Δ24 difference between the TBs of channels 183.31±1.8 and 183.31±4.5 GHz;

6. surface type (land, sea, coast);

7. TPW;

8. season;

9. surface height (altitude);

10. secant of the zenith angle.

The network architecture is similar to that of PNPR, with one input layer (with number of nodes equal to the number of inputs) and two hidden layers with 23 and 10 nodes, in the first and in the second layer respectively (the number of nodes differs from PNPR). The tan-sigmoid transfer function is used for the input and the hidden layers, while a linear transfer function is used for the output node.

**Fig. 08** shows the flow diagram of the PNPR v2 (H18) algorithm. The PNPR v2 algorithm receives as input the TBs (in BUFR or HDF format) measured by ATMS radiometer currently on board the Suomi-NPP satellite (and JPSS satellites as soon as available).

A first check (Brightness Temperatures Processing block) is carried out on the TBs, and pixels with any TB value less than 50 K or greater than 400 K are discarded and non considered for the retrieval; furthermore the three outmost pixels along the scan are discarded due to their low spatial resolution. A second step involves the generation of the auxiliary maps (Auxiliary Maps Generation block).

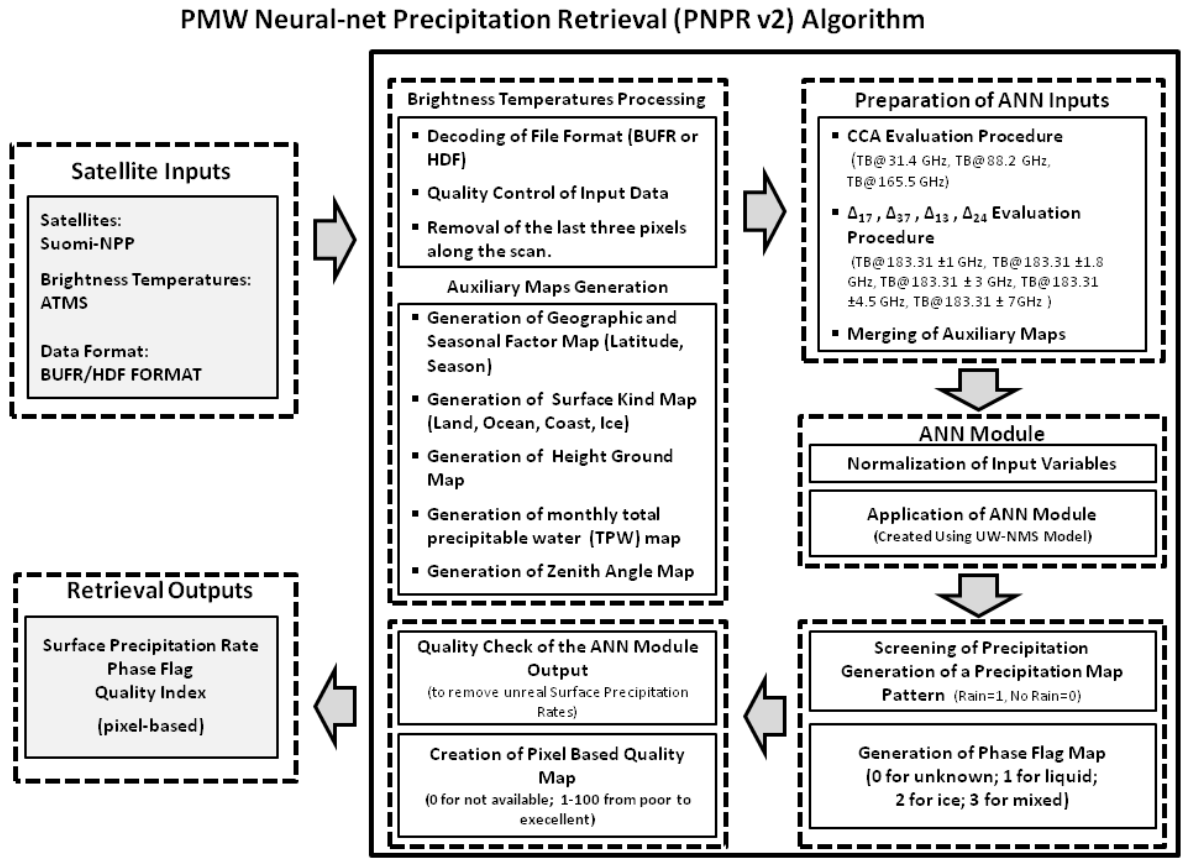


***Fig. 08*** Flow diagram of the PNPR v2 (H18) algorithm.

The algorithm generates five maps: the TPW map, the seasonal map, the surface type map (land, ocean, coast), the orography map (surface height) and the zenith angle map. The surface type map does not contain information on the presence of snow/ice at the surface. The identification of such

condition is assigned to the PNPR v2 algorithm itself. The third step (NN Inputs Processing block) concerns the evaluation of the NN inputs LCT, Δ17, Δ37, Δ13, Δ24. The fourth step (NN Module block) involves the normalization of the inputs and the application of the neural network to evaluate the pixel-based precipitation retrieval. In these blocks the NN inputs LCT, Δ17, Δ13, Δ37, and Δ24 are applied, together with the data of auxiliary maps to the NN. The surface precipitation rate is then evaluated by the NN. The fifth step (Screening of Precipitation block) involves a screening test for identification of potentially precipitating pixels. The precipitation map, obtained from the screening procedure, is used to filter the NN output (which includes all the pixels of the satellite swath) setting to zero the rain rate values of the pixels identified as "no rain". The sixth step (Generation of Phase Flag Map block) concerns the determination of the phase of the precipitation: liquid, solid, mixed or unknown (when the phase determination procedure is not applicable). The phase flag is evaluated only for pixels flagged as precipitating after the screening procedure and it is not available over coastal background surfaces. The precipitation phase is also used in the Quality Map definition. The seventh step (Quality Check of the ANN module Output) involves a pixel-based check to detect and remove the unreal value of precipitation (i.e. negative value) evaluated by the NN (the unreal value of NN precipitation resulted lower than 0.001% considering a one year statistical test over the H-SAF full disk area). In a subsequent step (Creation of Pixel Based Quality Map) the algorithm provides a quality flag to be associated to the retrieval, providing immediate indication of areas or conditions where the retrieval is more or less accurate. The quality flag (poor, fair, good, or missing) is based on a Percentage Confidence Index (PCI) describing both the product quality and reliability.

### *3.2.7 Quality Index and phase flag*

In the last step of the H18 product generation chain, a pixel based quality flag and a pixel based phase flag is computed.

***Phase of precipitation***

H18 provides a phase flag associated to the surface precipitation estimates. The phase flag is based on the studies on snow and ice detection of Surussavadee and Staelin (2009) and Rosencrantz (2003). In these studies snowfall is detected by the use of TBs at 20.3 GHz, 50.3 GHz and 89 GHz , and on combinations of these TBs. The phase identification procedure compares the selected TB's and their derived quantity with some thresholds to distinguish between liquid or iced precipitation, and to be able to detect falling snow over snowy or iced background. The thresholds are based on the use of AMSU-A and MHS/MHS channels, and these same thresholds are used for PR-OBS-2A (new rel., ver. 2.4).

With reference to Grody et al. (2000), the following index are used to identify the presence of snow and ice background:

| | | | |
|---|---|---|---|
| TT | = | $168+0.49\ TB_{89}$ | (over land) |
| Scattering index | = | $TB_{23}-TB_{89}$ | (over land) |
| Discriminate function | = | $5.1+0.078\ TB_{23}-0.096\ TB_{50}$ | (over ocean) |

The phase flag is evaluated only for pixels flagged as precipitating after the screening procedure and it is not available over coastal background surfaces.

The phase flag is given as an integer number according to the code table of the standard output field associated. The integers will be associated as follows:

| Phase flag | Integer value |
|---|---|
| unknown (flag determination not reliable) | 0 |
| Liquid | 1 |
| Ice | 2 |
| Mixed | 3 |
| missing value (bad data, or precipitation retrieval not available) | 7 |

**Table 09: Phase flag values and interpretation**

### *3.2.8 The quality index*

H18 algorithm provides a quality index to be associated to the estimated value of surface precipitation rate. The quality flag summarizes the product quality and reliability and provides the end-users with a simple and immediate criterion for the evaluation of the products towards a correct selection and application of the precipitation estimates with respect to the analyzed scenario. This index is derived from the "Percentage of Confidence Index" (PCI), evaluated on the base of four different criteria:

1) ***Quality of input data*** (used sensor, type and number of channels used, horizontal resolution, malfunctioning of radiometers);
2) ***Background surface index*** (type of surface, snowy background, presence of ice);
3) ***Event type index*** (snow storm, stratiform rain, convective cells);
4) ***Internal algorithm performance index*** (i.e., dependence on scan viewing angle).

The quality index and the PCI are connected as shown in the following table:

| Percentage of confidence index | Quality flag | Quality index |
|---|---|---|
| 0 | Missing data | 0 |
| 1-20 | Poor | 1 |
| 21-80 | Fair | 2 |
| 81-100 | Good | 3 |

**Table 06: Quality index values and interpretation and correspondence with percentage of confidence index (PCI).**

The PCI evaluation procedure is based on the following steps:

1. The output of the screening procedure is considered. For pixels without presence of rain a preliminary value of PCI is evaluated according to some conditions on the $TB^{max}_{53.6}$ (defined in the screening module, see Section 4.2):

| Test on TB | Environmental situation | Preliminary PCI |
|---|---|---|
| $TB_{53.6} < 242$ K | very cold/dry (not precipitating) | 0 |
| $TB_{53.6} >= 242$ K & $TB_{53.6} < 248$ K | cold/dry situation | 20 |
| $TB_{53.6} >= 248$ K | warm/wet situation | 50 |

**Table 07: Preliminary PCI thresholds based on screening algorithm.**

2. The presence of snow/ice on area without precipitation lowers the value of the PCI (the PCI value is limited to 10).

3. For rainy pixels the PCI value is based on a procedure that identifies the event typology. This procedure (Funatsu 2006, 2011) classifies the event in not identified/light stratiform, stratiform, convective, heavy convective (overshooting top) and associates a preliminary value of PCI according to the following table.

| Typology of event | Preliminary PCI |
|---|---|
| not identified/light stratiform | 40 |
| stratiform | 50 |
| convective | 90 |
| heavy convective | 90 |

**Table 08: Preliminary PCI based on precipitation type**

4. The presence of snow/ice on area with precipitation lowers the value of the PCI (the PCI value is limited to 10).
5. The PCI value associated to precipitation on coastal area is limited to 30 ("fair").
6. The preliminary PCI value is combined to some correction coefficients to become the final value of PCI:
   - satellite operation status coefficient (the PCI value decreases when satellite has some problem, i.e.. damaged channels, etc);
   - scan geometry coefficient (the value decreases as the scan angle increases);
   - not reliable data coefficient (the PCI is set to 0 in case of unrealistic value of measured TB's);

### *3.2.9 Algorithm validation/heritage*

H18 (PNPR v.2) represents an evolution, for ATMS applications, of previous H02A/B (PNPR) algorithm based on a NN approach, developed at ISAC-CNR for precipitation rate estimation using AMSU/MHS observations. The design procedure, common to PNPR is described in Sanò et al. (2015).

H02B is the extended version of the H02A to provide rainfall rate estimates for the MSG full disk area (LAT 60°S - 75°N, LON 60°W - 60°E). The product has been optimized for Europe and Mediterranean area (H-SAF area) and for Africa and Southern Atlantic. H02B is designed to provide the same rainfall estimates over the H-SAF area as those provided by H02A. The previous versions of the H02 were based on the algorithm of Surussavadee and Staelin (2008a, b), consisting of an artificial neural network (ANN) based precipitation retrieval algorithm for applications with measurements from AMSU-A and AMSU-B/MHS (AMSU-B is MHS's ancestor instrument on an earlier generation of NOAA POES satellites). They trained their algorithm through a database generated from cloud-radiation model (CRM) precipitation simulations. They used as their CRM basis, the Pennsylvania State University / National Center for Atmospheric Research (PSU/NCAR) Mesoscale Model-5 (MM5) described by Dudhia (1993) and Grell et al. (1994), with which they produced multiple simulations at a number of locations on the globe. Their algorithm includes particular corrections for limb-sounding effects, due to cross-track scanning, resolution enhancement techniques for AMSU-A data and techniques for precipitation screening purposes that are based on principal component analysis.
The main differences respect to PNPR are listed below:

1) H18 adopt a new fully redesigned single ANN trained using both the European and the African databases while H02A/B uses two NNs (ANN-A for European Area, ANN-B for African Area) trained by the two databases.
2) The exploitation of two new ATMS channels. Combined use of the new 183±1.8 and 183±4.5 GHz channels with the previous AMSU-MHS used channels.
3) The use of monthly mean TPW (ECMWF reanalysis 2011-2014 period used for training the ANN) to drive ANN in the transition between the European and African area.

Currently H18 is found to perform reasonably well (within the H-SAF area) over sea and vegetated land for all types of precipitation as evaluated against radar data relatively to some selected case studies.

A verification study over Africa and Southern Atlantic has been carried out over a two-year period (2013-2014) using the TRMM Precipitation Radar as reference (NASA TRMM standard product 2A25 version 7). The comparison between ATMS and PR retrievals is based on a two-year coincidence dataset of ATMS and PR observations (within a 15 min time window) over the area of interest, in the years 2013-2014, considering all TRMM satellite and the SUOMI-NPP satellite orbits.

Over Africa and Southern Atlantic the performance are good over all types of surfaces with Root Mean Square Error (RMSE) between 0.80 mm/h (arid land) and 1.37 mm/h (coast), Correlation Coefficient (CC) between 0.71 (vegetated land) and 0.64 (arid land) and Mean Error (ME) between 0.05 (arid land, coast and ocean areas) and 0.08 (vegetated land) (see Puca et al., 2014 for the definition of the statistical scores). The statistical analysis has been carried out over a regular grid at 0.5° × 0.5° resolution.

# 4 Examples of H18 products

**Fig. 09, Fig.10, Fig. 11,** and **Fig. 12** show examples of ATMS measurements at 165 GHz, and H18 rainfall rate maps, with quality map associated.

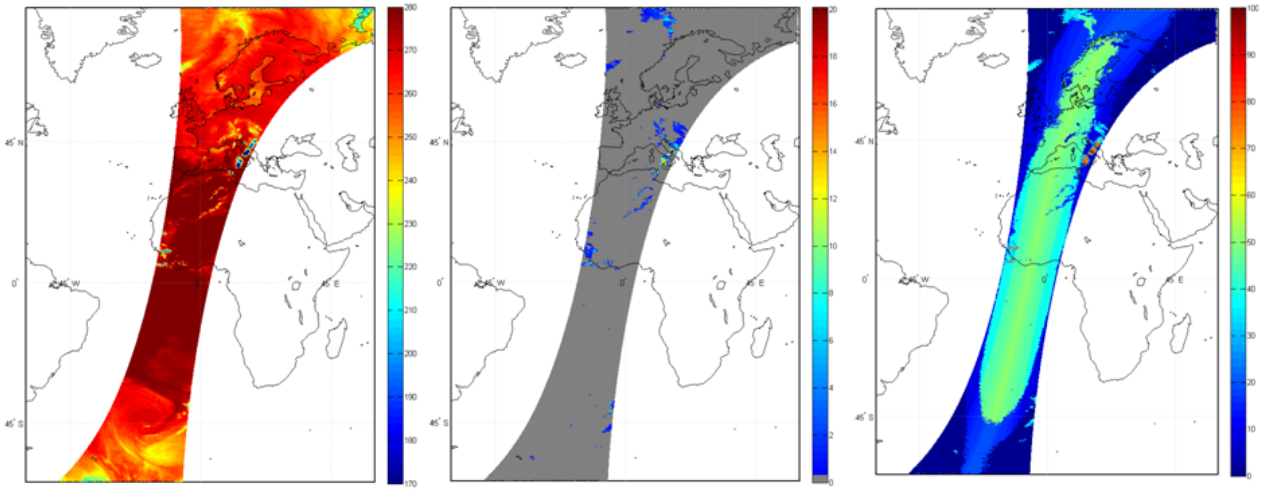

***Fig. 09 - Example of a 165 GHz image for ATMS orbit over the MSG full disk area* (LAT 60°S - 75°N, LON 60°W - 60°E) *(left panel) and H18 rainfall rate (mm/h) (centre panel) and quality index (right panel) - Satellite Suomi-NPP, Day 14 October 2015, 22:10 UTC***

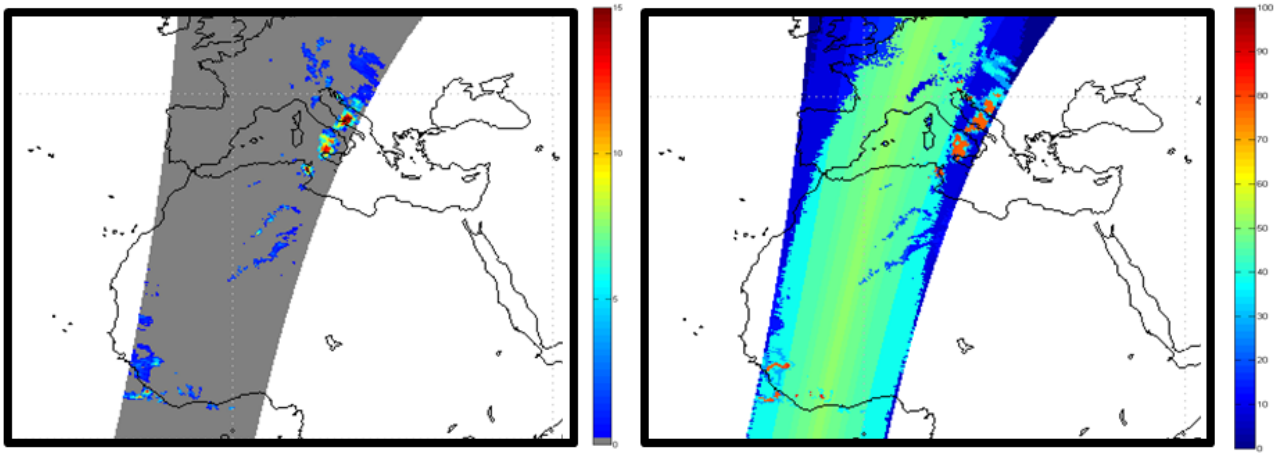

***Fig. 10 – Detail of Fig. 09, with H18 rainfall rate (mm/h) (left panel) and quality index (right panel)- Satellite Suomi-NPP, Day 14 October 2015, 22:10 UTC***

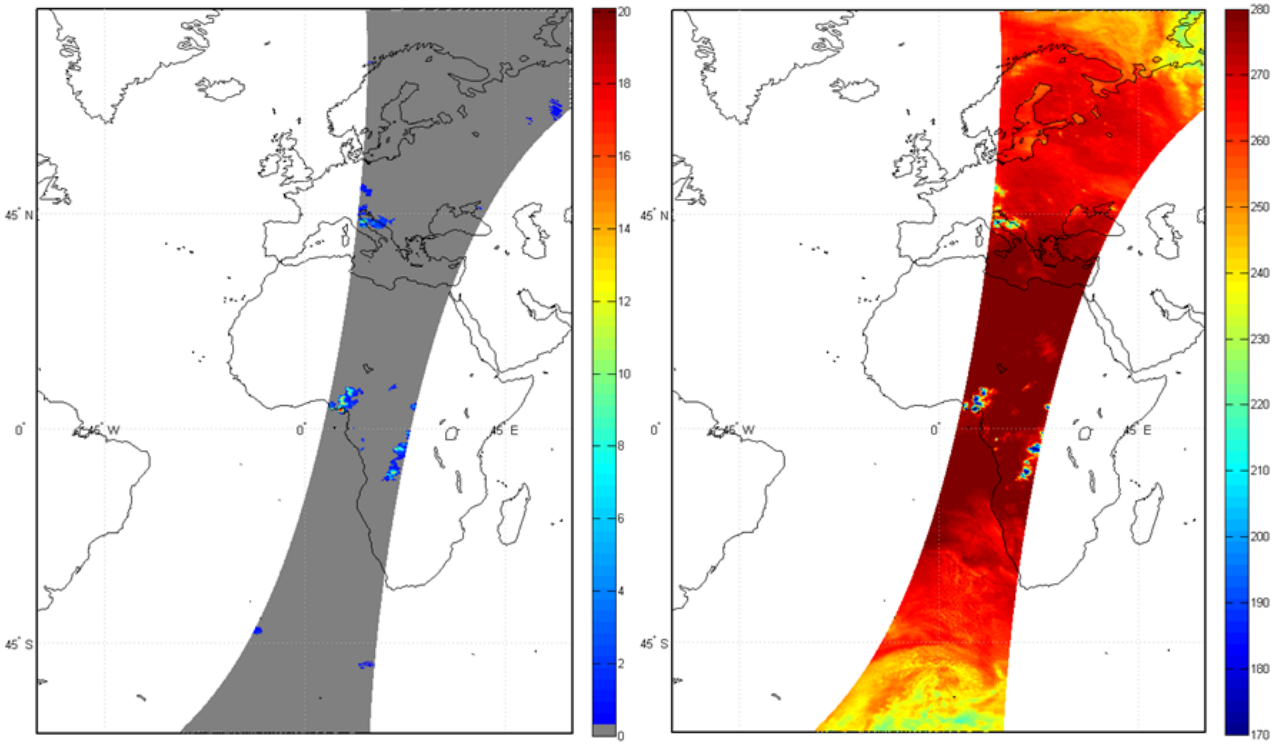


***Fig. 11 – H18 rainfall rate (mm/h) (left panel) and Tb 165 GHz (right panel: Convective events over Italy and African regions - Satellite Suomi-NPP, Day 13 October 2015, 10:09 UTC***

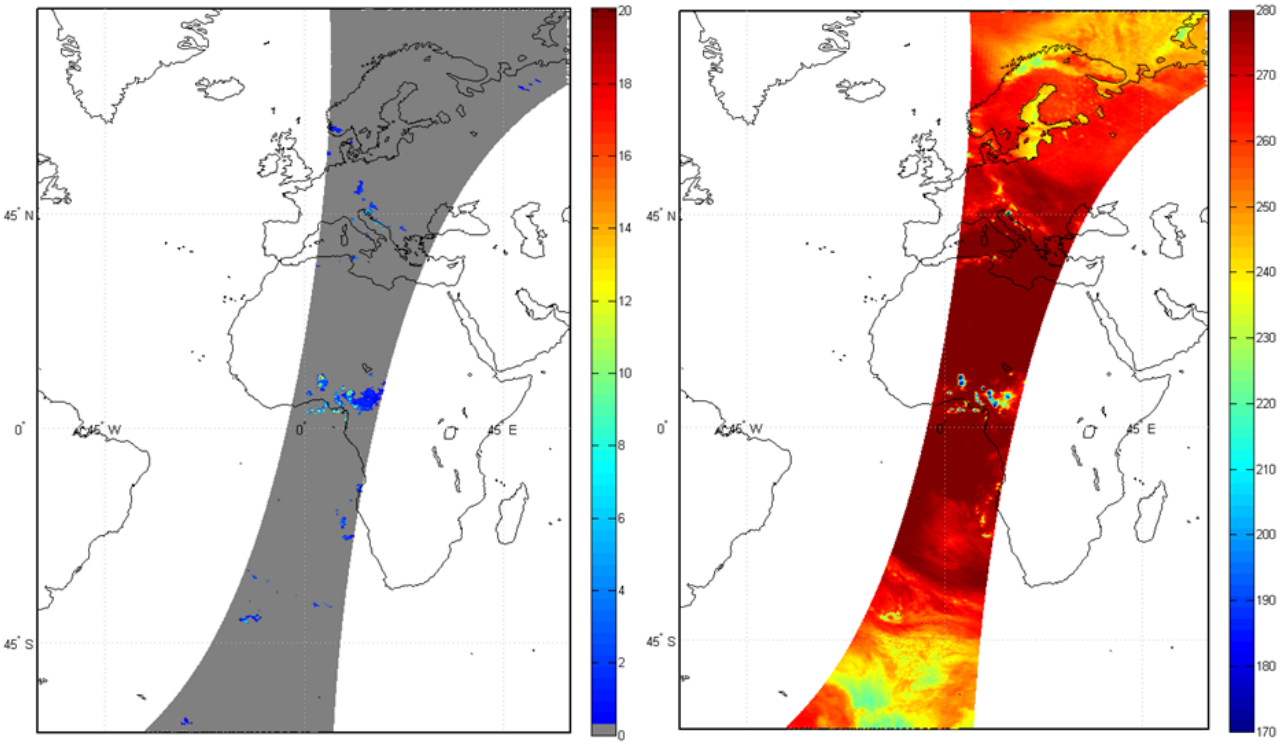


*Fig. 12 - Same as Fig. 11: Convective event over African regions - Satellite Suomi-NPP, Day 02 December 2014, 07:16 UTC*

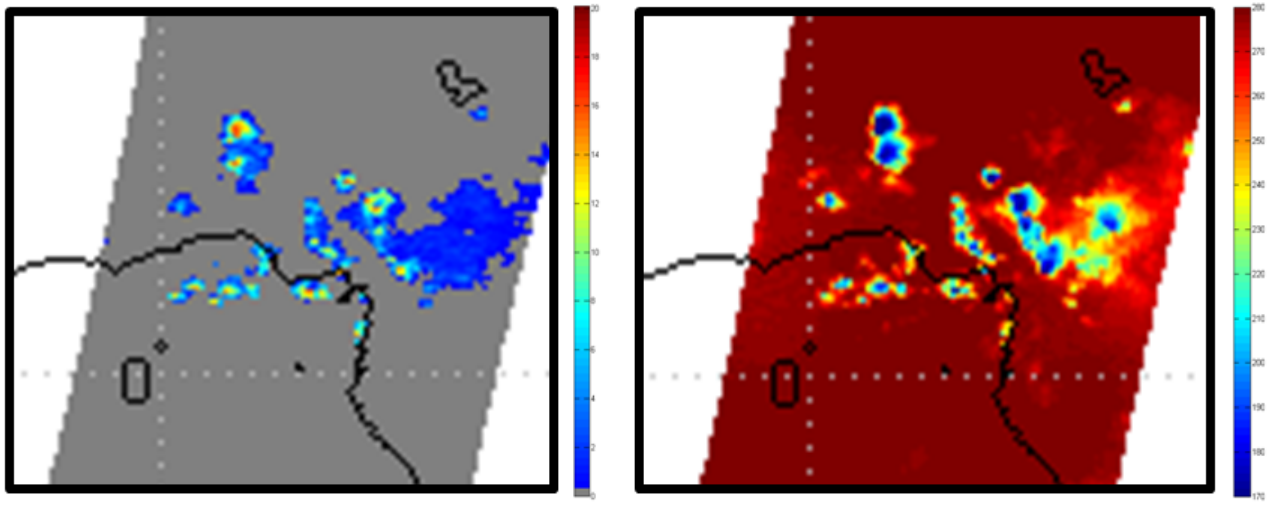

*Fig. 13 – Detail of Fig. 12, with H18 rainfall rate (mm/h) (left panel) and Tb 165 GHz (right panel)- Satellite Suomi-NPP, Day 02 December 2014, 07:16 UTC*

# 5 Applicable documents

1- CDOP2 PRD – H-SAF CDOP2 Product Requirement Document Rel. 1.2, Ref: SAF/HSAF/CDOP2/PRD/1.2

# 6 References

Anders, U. and Korn, O. "Model selection in neural networks", Neural Netw., 12, 309-323, 1999.

Bellerby, T.J.: Satellite rainfall uncertainty estimation using an artificial neural network, J. Hydrometeorol., 8, 1397-1412, 2007.

Bauer, P., E. Moreau, F. Chevallier, and U. O'Keeffe, "Multiple-scattering microwave radiative transfer for data assimilation applications," *Q. J. Roy. Meteor. Soc.,* vol. 132, pp. 1259-1281, Apr 2006.

Bennartz, R.: Optimal convolution of MHS to AMSU-A, J. Atmos. Oceanic Tech., 17, 1215-1225, 2000.

Bennartz, R. and Petty, G. W.: The sensitivity of microwave remote sensing observations of precipitation to ice particle size distributions, J. Appl. Meteorol., 40, 345-364, 2001.

Blackwell, W.J. and Chen, F.W.: Neural network applications in high-resolution atmospheric remote sensing, Lincoln Lab. J., 15, 299-322, 2005.

Casella, D., Panegrossi, G., Sanò, P., Mugnai, A., Smith, E.A., Tripoli, G.J., Dietrich, S., Formenton, M., Di Paola, F., Leung, H. W.-Y., and Mehta, A.V.: Transitioning from CRD to CDRD in Bayesian retrieval of rainfall from satellite passive microwave measurements, Part 2: Overcoming database profile selection ambiguity by consideration of meteorological control on microphysics, IEEE Trans. Geosci. Remote Sens, vol.51, no.9, 4650-4671, doi: 10.1109/TGRS.2013.2258161, 2013

Casella, D., Panegrossi, G., Sanò, P., Milani, L., Petracca, M., and Dietrich, S.: A novel algorithm for detection of precipitation in tropical regions using PMW radiometers, Atmos. Meas. Tech., 8, 1217-1232, doi:10.5194/amt-8-1217-2015, 2015.

Chen F.W. and D.H. Staelin, 2001: "Millimeter-Wave Observations of Precipitation Using AMSU on the NOAA-15 Satellite". *Proc. of the 2001 IEEE International Geoscience and Remote Sensing Symposium*, 9-13 July 2001, vol. 3, pp. 1044-1045.

Chen F.W. and D.H. Staelin, 2002: "Millimeter-wave observation of precipitation using AMSU on the NOAA-15 satellite". *Proc. of the 2002 Int. Geoscience and Remote Sensing Symposium*, Toronto, 24-28 June 2002, vol. 1, 460-462.

Chen F.W. and D.H. Staelin, 2003: "AIRS/AMSU/HSB Precipitation Estimates". *IEEE Transactions on Geoscience and Remote Sensing*, vol. 41, no. 2, pp. 410-417.

Chen F.W., 2004: "Global Estimation of Precipitation Using Opaque Microwave Bands". Ph.D. thesis, MIT.

Chen, Y., Aires, F., Francis, J. A., and Miller, J. R.: Observed relationships between artic longwave cloud forcing and cloud parameters using a neural network, J. Climate, 4087-4104, 2006.

Cotton W.R., G.J. Tripoli, R.M. Rauber and E.A. Mulvihill, 1986: "Numerical Simulation of the effects of varying ice crystal nucleation rate and aggregation processes on orographic snowfall". *J. Clim. Apl. Meteor.* 25**:** 1658-1680.

Cotton W.R., M.A. Stephens, T. Nehrkorn and G.J. Tripoli, 1982: "The Colorado State University three-dimensional cloud / mesoscale model-1982. Part II: An ice phase parameterization". *J. Rech. Atmos.* 16: 295-320.

Deirmendjian D., 1969: "*Electromagnetic Scattering on Spherical Polydispersions*". American Elsivier Publishing Co., New York, NY.

Dudhia, J.: A nonhydrostatic version of the Penn State-NCAR Mesoscale Model: Validation tests and simulation of an Atlantic cyclone and cold front, Mon. Wea. Rev., 121, 1493-1513, 1993.

Flatau P., G.J. Tripoli, J. Berlinde and W. Cotton, 1989: "The CSU RAMS Cloud Microphysics Module: General Theory and Code Documentation". *Technical Report 451*, Colorado State University, 88 pp.

Funatsu, B. M., V. Dubreuil, C. Claud, D. Arvor, and M. A. Gan (2012), Convective activity in Mato Grosso state (Brazil) from microwave satellite observations: Comparisons between AMSU and TRMM data sets, J. Geophys. Res., 117, D16109, doi:10.1029/2011JD017259

Funatsu, B. M., C. Claud, and J.-P. Chaboureau (2007), Potential of Advanced Microwave Sounding Unit to identify precipitating systems and associated upper-level features in the Mediterranean region: Case studies, J. Geophys. Res., 112, D17113, doi:10.1029/2006JD008297

Gasiewski A.J., 1988: "Atmospheric Temperature Sounding and Precipitation Cell Parameter Estimation Using Passive 118-GHz O2 Observations". Ph.D. thesis, Department of Electrical Engineering and Computer Science, MIT.

Gasiewski A.J., 1993: "Microwave Radiative Transfer in Hydrometeors". In *Atmospheric Remote Sensing by Microwave Radiometry* (edited by M.A. Janssen), John Wiley & Sons, Inc., New York, NY.

Goldberg M.D. and H.E. Fleming, 1995: "An Algorithm to Generate Deep-Layer Temperatures from Microwave Satellite Observations for the Purpose of Monitoring Climate Change". *Journal of Climate* **8**: 993-1004.

Goldberg M.D., D.S. Crosby and L. Zhou, 2001: "The Limb Adjustment of AMSU A Observations: Methodology and validation". *Journal of Applied Meteorology*, 40, 70-83.

Grell, G., Dudhia, J., and Stauffer, D. R.: A Description of the Fifth Generation Penn State/NCAR Mesoscale Model (MM5), NCAR Techical Note NCAR/TN-398+STR, National Center for Atmospheric Research, Boulder, Colorado, USA, 121 pp., 1994.

Grenfell T.C. and S.G. Warren, 1999: "Representation of a nonspherical ice particle by a collection of independent spheres for scattering and absorption of radiation". *J. Geophys. Res.*, **104**, 31697-31709.

Groody N., F. Weng and R. Ferraro, Application of AMSU for obtaining hydrological parameters, Microwave Radiometry and Remote Sensing of the Earth's Surface and Atmosphere, P. Pampaloni, S. Paloscia , eds.: VSP, 2000. pp.339-352.

Hall D.L. and J. Llinas, 1997: "An Introduction to Multisensor Data Fusion". *Proc. of the 1997 IEEE*, vol. 85, no. 1, 6-23.

Haykin, S.O.: Neural Networks: A Comprehensive Foundation, 2nd Edition, Prentice Hall, 842 pp., 1998.

Haykin, S.O.: Neural Networks and Learning Machines, 3rd Edition. Prentice Hall, 906 pp., 2009.

Hewison T.J., 2001: "Airborne measurements of forest and agricultural land surface emissivity at millimeter wavelengths". *Geoscience and Remote Sensing*, IEEE Transactions, vol. 39, issue 2, 393-400.

Hewison T.J. and S.J. English, 1999: **"**Airborne retrievals of snow and ice surface emissivity at millimeter wavelengths". *Geoscience and Remote Sensing*, IEEE Transactions. vol. 37, issue 4, 1871-1879.

Hewison, T. and S. English, 2000: "Fast models for land surface emissivity". In *Radiative Transfer Models for Microwave Radiometry* (C. Matzler, ed.), COST Action 712, Directorate-General for Research, European Commission, Brussels, Belgium, 117-127.

Hong, G., Heygster, G., Miao, J., and Kunzl, K.: Detection of tropical deep convective clouds from AMSU-B vater vapour channels measurements, J. Geophys. Res., 110, D05205, doi:10.1029/2004JD004949, 2005.

Hou, A. Y., Kakar, R. K., Neeck, S., Azarbarzin, A. A., Kummerow, C. D., Kojima, M., Oki, R., Nakamura, K., and Iguchi, T.: "The global precipitation measurement mission", B. Am. Meteorol. Soc., 95, 701-722, doi:10.1175/BAMS-D-13-00164.1, 2014.

Hsu, K.-L., Gao, X., Sorooshian, S., and Gupta, H. V., Precipitation estimation from remotely sensed information using artificial neural networks, J. Appl. Meteorol., 36, 1176-1190, 1997.

Hufford G., 1991: "A Model for the Complex Permittivity of Ice at Frequencies Below 1 THz". International *Journal of Infrared and Millimeter Waves*, Vol. 12, No. 7, 677-682.

Karkkainen K., A. Shivola and K. Nikoskinen, 2001 "Analysis of a three-dimensional dielectric misture with finite difference method". IEEE Trans. Geosci. Remote. Sens 39, 1013-1018.

Kedem B., H. Pavlopoulos, X. Guan and D.A. Short, 1994: "A Probability Distribution Model for Rain Rate". Journal of Applied Meteorology, vol. 33, no. 12, 1486-1493, Dec. 1994.

Kidd, C., Matsui, T., Chern, J., Mohr, K., Kummerow, C. and Randel, D., 2016: Global Precipitation Estimates from Cross-Track Passive Microwave Observations Using a Physically Based Retrieval Scheme" in the Journal of Hydrometeorology 17, 1. DOI: 10.1175/JHM-D-15-0051.1

Kirstetter, P. E., Hong, Y., Gourley, J. J., Chen, S., Flamig, Z., Zhang, J., Schwaller, M., Petersen, W., Amitai, E.:Toward a Framework for Systematic Error Modeling of Spaceborne Precipitation Radar with NOAA/NSSL Ground Radar–Based National Mosaic QPE, Journal of Hydrometeorology, Volume 13, Issue 4, pp. 1285-1300 , doi: http://dx.doi.org/10.1175/JHM-D-11-0139.1, 2012.

Kulie, M. S., R. Bennartz, T. J. Greenwald, Y. Chen, and F. Z. Weng, "Uncertainties in Microwave Properties of Frozen Precipitation Implications for Remote Sensing and Data Assimilation," *J. Atmos. Sci.,* vol. 67, pp. 3471-3487, Nov 2010

Kummerow, C. D., S. Ringerud, J. Crook, D. Randel, and W. Berg, "An observationally generated a priori database for microwave rainfall retrievals," J. Atmos. Ocean. Technol., vol. 28, no. 2, pp. 113–130, 2011.

Kummerow, C. D. D. L. Randel, M. Kulie, N. Wang, R. Ferraro, S. J. Munchak, and V. Petkovic, 2015: The Evolution of the Goddard Profiling Algorithm to a Fully Parametric Scheme. J. Atmos. Oceanic Technol., 32, 2265–2280.

Lippmann R.P., 1987: "An Introduction to Computing with Neural Nets". IEEE Acoustics, Speech, and Signal Processing Magazine, vol. 4, no. 2, 4-22.

Liebe H.J. and G.G. Gimmestad, 1978: "Calculation of clear air EHF refractivity". *Radio Sci*., **13**, 245-251.

Liebe H.J., 1985: "An updated model for millimeter wave propagation in moist air". *Radio Sci*., **20**, 1069-1089.

Liou, K., *An Introduction to Atmospheric Radiation (2nd Edition)* vol. 84: Academic Press, 2002.

Liu Q., C. Simmer and E. Ruprecht, 1996: "Three-dimensional radiative transfer effects of clouds in the microwave spectral range". *J. Geophys. Res*., **101**, 4289-4298.

Marzban C. "Basic statistics and basic AI: neural networks, in: Artificial Intelligence Methods in the Environmental Science" edited by: Haupt, S.E., Pasini, A., and Marzban C., Springer, 15-47, 2009.

MHS: Advanced Microwave Sounding Unit-A (AMSU-A), NOAA KLM User's Guide, Section 3.3, NOAA National Environmental and Data Information Service, National Climatic Data Center, [http://www.ncdc.noaa.gov/oa/pod-guide/ncdc/docs/klm/cover.htm], 2009.

Mugnai A., D. Casella, E. Cattani, S. Dietrich, S. Laviola, V. Levizzani, G. Panegrossi, M. Petracca, P. Sanò, F. Di Paola, D. Biron, L. De Leonibus, D. Melfi, P. Rosci, A. Vocino, F. Zauli, S. Puca, A. Rinollo, L. Milani, F. Porcù, and F. Gattari: Precipitation products from the Hydrology SAF, Nat. Hazards Earth Syst. Sci., 13, 1959-1981, doi:10.5194/nhess-13-1959-2013, 2013a.

Mugnai A., E. A. Smith, G. J. Tripoli, B. Bizzarri, D. Casella, S. Dietrich, F. Di Paola, G. Panegrossi, P. Sanò, CDRD and PNPR Satellite Passive Microwave Precipitation Retrieval Algorithms: EuroTRMM / EURAINSAT Origins and H-SAF Operations, Nat. Hazards Earth Syst. Sci., 13, 887-912, doi:10.5194/nhess-13-887-2013, 2013b.

Panegrossi, G., Dietrich, S., Marzano, F.S., Mugnai, A., Smith, E.A., Xiang, X., Tripoli, G.J., Wang, P.K., and Poiares Baptista, J.P.V.: Use of cloud model microphysics for passive microwave-based precipitation retrieval: Significance of consistency between model and measurement manifolds, J. Atmos. Sci., 55, 1644-1673, 1998.

Panegrossi, G., "Validation of Microphysics Parameterization in Cloud Resolving Models using Passive Microwave Measurements," Ph.D. Dissertation, Univ. of Wisconsin, Madison, WI, UW MET Publication No.04.00.P1, 2004.

Panegrossi G., Sanò P., D. Casella, S. Dietrich, M. Petracca, A. Mugnai, A verification study over Europe of AMSU-A/MHS and SSMIS passive microwave precipitation retrievals, Proc. 2013 EUMETSAT/AMS Meteorol. Sat. Conference, Vienna, Sept. 2013

Panegrossi G., Sanò P., D. Casella, S. Dietrich, L. Milani, M. Petracca, A. Mugnai, CDRD and PNPR passive microwave precipitation retrieval algorithms: extension to the MSG full disk area within H-SAF, Proc. 2014 EUMETSAT/AMS Meteorol. Sat. Conference, Geneva, Sept. 2014

Pohl C. and J.L. van Genderen, 1998: "Multisensor Image Fusion in Remote Sensing: Concepts, Methods, and Application". International Journal of Remote Sensing, vol. 19, no. 5, pp. 823-854, 1998.

Prigent C, Aires F, Rossow WB. 2006. Land surface microwave emissivities over the globe for a decade. Bull. Am. Meteorol. Soc. 87: 1573–1584. DOI:10.1175/BAMS-87-11-1573.

Roberti L., J. Haferman and C. Kummerow, 1994: "Microwave radiative transfer through horizontally inhomogeneous precipitating clouds". J. Geophys. Res., **99**, 16707-16718.

Rosenkranz, P., 2003: Rapid Radiative Transfer Model for AMSU/HSB Channels, IEEE Trans. Geosci. Rem. Sens., 41, 362-368.

Sanò, P., Casella, D., Mugnai, A., Schiavon, A., Smith, E.A., and Tripoli, G.J.: Transitioning from CRD to CDRD in Bayesian retrieval of rainfall from satellite passive microwave measurements, Part 1: Algorithm description and testing, IEEE Trans. Geosci. Remote Sens., Vol. 51, no. 7, 4119-4143, doi: 10.1109/TGRS.2012.2227332, 2013.

Sanò, P., Panegrossi, G., Casella, D., Di Paola, F., Milani, L., Mugnai, A., Petracca, M., and Dietrich, S.: The Passive microwave Neural network Precipitation Retrieval (PNPR) algorithm for AMSU/MHS observations: description and application to European case studies, Atmos. Meas. Tech., 8, 837-857, doi:10.5194/amt-8-837-2015, 2015.

Shi, L.: Retrieval of atmospheric temperature profiles from AMSU-A measurement using a neural network approach, J. Atmos. Ocean. Tech., 18, 340-347, 2001.

Smith, E. A., P. Bauer, F. S. Marzano, C. D. Kummerow, D. McKague, A. Mugnai, and G. Panegrossi, "Intercomparison of microwave radiative transfer models for precipitating clouds," IEEE Trans. Geosci. Remote Sens, vol. 40, pp. 541-549, 2002.

Smith E.A., Hester W.-Y. Leung, James B. Elsner, Amita V. Mehta, Gregory J. Tripoli,Daniele Casella, Stefano Dietrich, Alberto Mugnai, Giulia Panegrossi, Paolo Sanò: Transitioning from CRD to CDRD in Bayesian Retrieval of Rainfall from Satellite Passive Microwave Measurements: Part 3. Identification of Optimal Meteorological Tags, Nat. Hazards Earth Syst. Sci., 13, 1185-1208, doi:10.5194/nhess-13-1185-2013, 2013.

Shivola A., 1989: "Self-Consistency Aspects of Dielectric Mixing Theories". *IEEE Trans. Geosci. Remote. Sens*. 27, 403-415.

Schlűssel P. and H. Luthardt, 1991, "Surface Wind Speeds Over the North Sea From Special Sensor Microwave/Imager Observations". *J. Geophys. Res*., vol. 96, No. C3, 4845-4853.

Spina M.S., M.J. Schwartz, D.H. Staelin and A.J. Gasiewski, 1998: "Application of Multilayer Feedforward Neural Networks to Precipitation Cell-Top Altitude Estimation". *IEEE Transactions on Geoscience and Remote Sensing*, vol. 36, no. 1, 154-162.

Staelin D.H, F.W. Chen and A. Fuentes, 1999: "Precipitation Measurements Using 183 GHz AMSU Satellite Observations". *Proc. of the 1999 IEEE International Geoscience and Remote Sensing Symposium*, vol. 4 , 2069-2071.

Staelin D.H. and F.W. Chen, 2000: "Precipitation Observations Near 54 and 183 GHz Using the NOAA-15 Satellite". *IEEE Transactions on Geoscience and Remote Sensing*, vol. 38, no. 5, 2322-2332.

Surussavadee C., 2006: "Passive Millimeter-Wave Retrieval of Global Precipitation Utilizing Satellites and a Numerical Weather Prediction Model". *Graduation thesis*, MIT Department of Electrical Engineering and Computer Science.

Surussavadee C. and D.H. Staelin, 2006: "Comparison of AMSU millimeterwave satellite observations, MM5/TBSCAT predicted radiances, and electromagnetic models for hydrometeors". *IEEE Trans. Geosci. Remote Sens.*, 44, 2667-2678.

Surussavadee, C., and Staelin, D.H.: Global millimeter-wave precipitation retrievals trained with a cloud-resolving numerical weather prediction model, Part I: Retrieval design, IEEE Trans. Geosci. Remote Sens., 46, 99-108, 2008a.

Surussavadee, C., and Staelin, D.H.: Global millimeter-wave precipitation retrievals trained with a cloud-resolving numerical weather prediction model, Part II: Performance evaluation, IEEE Trans. Geosci. Remote Sens., 46, 109-118, 2008b.

Surussavadee, C, and David H. Staelin, 2009: Satellite retrievals of Arctic and Equatorial rain and snowfall rates using millimeters wavelengths, IEEE Trans. Geosci. Rem. Sens., 47, 3697-3707.

Tang, L., et al., An improved procedure for the validation of satellite-based precipitation estimates, Atmos. Res., http://dx.doi.org/10.1016/j.atmosres.2014.12.016, 2015

Tripoli G.J. and W.R. Cotton, 1981: "The use of ice-liquid water potential temperature as a thermodynamic variable in deep atmospheric models". *Mon. Wea. Rev.*, **109,** 1094-1102.

Tripoli G.J. and W.R. Cotton, 1982: "The Colorado State University three-dimensional cloud / mesoscale model-1982. Part I: General theoretical framework and sensitivity experiments". *J. Rech. Atmos*. **16:** 185-200.

Tripoli G.J. and W.R. Cotton, 1986: "An intense, quasi-steady thunderstorm over mountainous terrain, part IV: three-dimensional numerical simulation". *J. Atmos. Sci*., **43,** 894-912.

Tripoli G.J., 1992a: "A non-hydrostatic model designed to simulate scale interaction". *Mon. Wea. Rev.*, **120**, 1342-1359.

Tripoli G.J., 1992b: "An explicit three-dimensional non-hydrostatic numerical simulation of a tropical cyclone". *Meteor. Atmos. Phys.*, **49**, 229-254.

Tripoli G. J. and Smith E.A., 2014: "Introducing variable-step topography (VST) coordinates in dynamically constrained, scalable, nonhydrostatic atmospheric models: Review of rationale and solutions on classical obstacle flow calibration problems. ," *Dyn. Atmos. Oceans,* **66** (2014) 28-57.

Tsai V.J.D, 2003: "Frequency-Based Fusion of Multiresolution Images". *Proc. of the 2003 IEEE International Geoscience and Remote Sensing Symposium*, vol. 6, 3665-3667.

Ulaby F.T., R.K. Moore and A.K. Fung, 1981: "*Microwave Remote Sensing: Active and Passive*", Addison-Wesley Pub. Co., Reading, MA.

Wald L., 1999: "Some Terms of Reference in Data Fusion". *IEEE Transactions on Geoscience and Remote Sensing*, vol. 37, no. 3, 1190-1193.

Wark D.Q., 1993: "Adjustment of TIROS operational vertical sounder data to a vertical view". *NOAA Tech. Rep. NESDIS-64*, 36 pp.

Weng F., X. Zou, X. Wang, S. Yang, M. D. Goldberg, 2012: "Introduction to Suomi national polar-orbiting partnership advanced technology microwave sounder for numerical weather prediction and tropical cyclone applications". JOURNAL OF GEOPHYSICAL RESEARCH, vol. 117, D19112, doi:10.1029/2012JD018144

Zou X., 2014: "Absolute Calibration of ATMS Upper Level Temperature Sounding Channels Using GPS RO Observations" IEEE Transactions on Geoscience and Remote Sensing, vol. 52, no. 02, 1397-1406.

# Annex 1: Introduction to H-SAF

## *The EUMETSAT Satellite Application Facilities*

H-SAF is part of the distributed application ground segment of the "*European Organization for the Exploitation of Meteorological Satellites (EUMETSAT)*". The application ground segment consists of a "*Central Application Facilities*" located at EUMETSAT Headquarters, and a network of eight "*Satellite Application Facilities (SAFs)*", located and managed by EUMETSAT Member States and dedicated to development and operational activities to provide satellite-derived data to support specific user communities (see Figure 19):

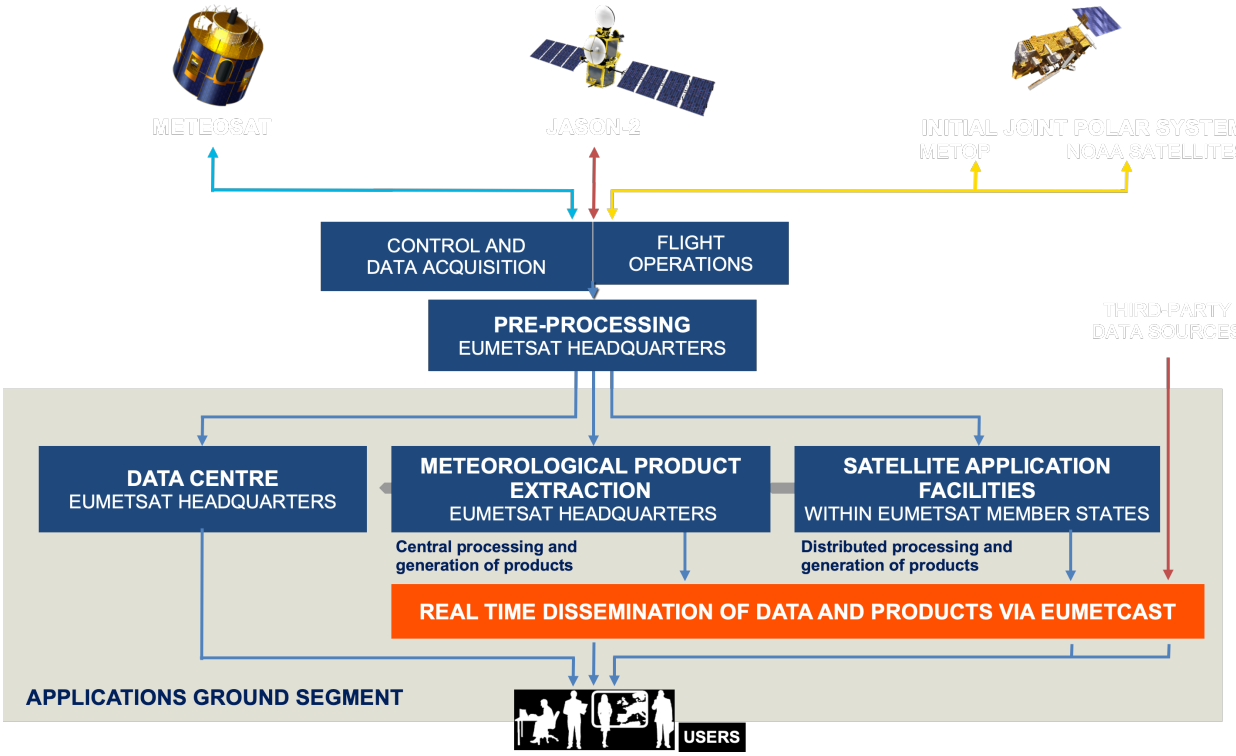


**Figure 13: Conceptual scheme of the EUMETSAT Application Ground Segment**

Figure 20 depicts the composition of the EUMETSAT SAF network, with the indication of each SAF's specific theme and Leading Entity.

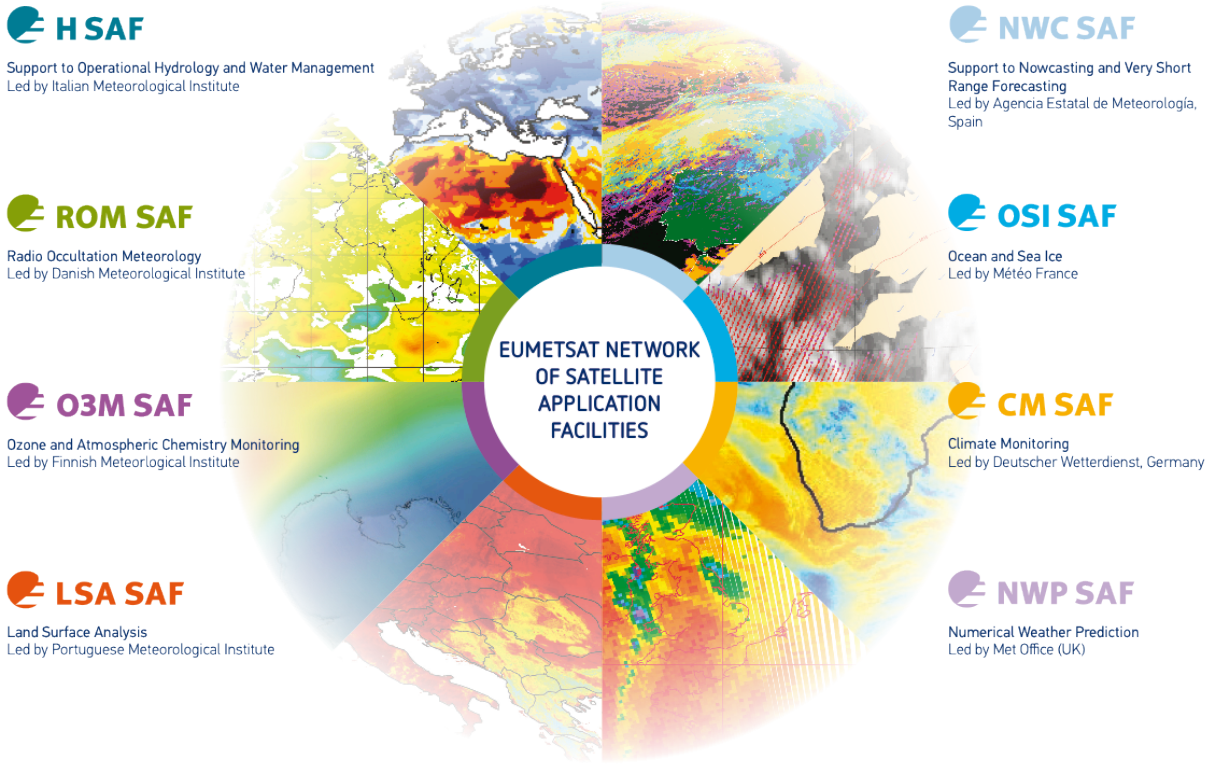


**Figure 14: Current composition of the EUMETSAT SAF Network**

### *Purpose of the H-SAF*

The main objectives of H-SAF are:

***a.*** ***to provide new satellite-derived products*** from existing and future satellites with sufficient time and space resolution to satisfy the needs of operational hydrology, by generating, centralizing, archiving and disseminating the identified products:

- precipitation (liquid, solid, rate, accumulated);
- soil moisture (at large-scale, at local-scale, at surface, in the roots region);
- snow parameters (detection, cover, melting conditions, water equivalent);

***b.*** ***to perform independent validation of the usefulness of the products*** for fighting against floods, landslides, avalanches, and evaluating water resources; the activity includes:

- downscaling/upscaling modelling from observed/predicted fields to basin level;
- fusion of satellite-derived measurements with data from radar and raingauge networks;
- assimilation of satellite-derived products in hydrological models;
- assessment of the impact of the new satellite-derived products on hydrological applications.

### *Products / Deliveries of the H-SAF*

For the full list of the Operational products delivered by H-SAF, and for details on their characteristics, please see H-SAF website hsaf.meteoam.it.
All products are available via EUMETSAT data delivery service (EUMETCast, http://www.eumetsat.int/website/home/Data/DataDelivery/EUMETCast/index.html), or via ftp download; they are also published in the H-SAF website hsaf.meteoam.it.
All intellectual property rights of the H-SAF products belong to EUMETSAT. The use of these products is granted to every interested user, free of charge. If you wish to use these products, EUMETSAT's copyright credit must be shown by displaying the words "copyright (year) EUMETSAT" on each of the products used.

### *System Overview*

H-SAF is lead by the Italian Air Force Meteorological Service (ITAF USAM) and carried on by a consortium of 21 members from 11 countries (see website: hsaf.meteoam.it for details)
Following major areas can be distinguished within the H-SAF system context:

- Product generation area
- Central Services area (for data archiving, dissemination, catalogue and any other centralized services)
- Validation services area which includes Quality Monitoring/Assessment and Hydrological Impact Validation.

Products generation area is composed of 5 processing centres physically deployed in 5 different countries; these are:

- for precipitation products: ITAF COMET (Italy)
- for soil moisture products: ZAMG (Austria), ECMWF (UK)
- for snow products: TSMS (Turkey), FMI (Finland)

Central area provides systems for archiving and dissemination; located at ITAF COMET (Italy), it is interfaced with the production area through a front-end, in charge of product collecting.
A central archive is aimed to the maintenance of the H-SAF products; it is also located at ITAF COMET.
Validation services provided by H-SAF consists of:

- Hydrovalidation of the products using models (hydrological impact assessment);
- Product validation (Quality Assessment and Monitoring).

Both services are based on country-specific activities such as impact studies (for hydrological study) or product validation and value assessment.
Hydrovalidation service is coordinated by IMWM (Poland), whilst Quality Assessment and Monitoring service is coordinated by DPC (Italy): The Services' activities are performed by experts from the national meteorological and hydrological Institutes of Austria, Belgium, Bulgaria, Finland, France, Germany, Hungary, Italy, Poland, Slovakia, Turkey, and from ECMWF.

# Annex 2: Acronyms

| | |
|---|---|
| AMSU | Advanced Microwave Sounding Unit (on NOAA and MetOp) |
| AMSU-A | Advanced Microwave Sounding Unit - A (on NOAA and MetOp) |
| ATMS | Advanced Technology Microwave Sounder |
| MHS | Advanced Microwave Sounding Unit - B (on NOAA up to 17) |
| ATDD | Algorithms Theoretical Definition Document |
| AU | Anadolu University (in Turkey) |
| BfG | Bundesanstalt für Gewässerkunde (in Germany) |
| CAF | Central Application Facility (of EUMETSAT) |
| CDOP | Continuous Development-Operations Phase |
| CESBIO | Centre d'Etudes Spatiales de la BIOsphere (of CNRS, in France) |
| CM-SAF | SAF on Climate Monitoring |
| COMET | Centro Operativo per la Meteorologia (in Italy) |
| CNR | Consiglio Nazionale delle Ricerche (of Italy) |
| CNRS | Centre Nationale de la Recherche Scientifique (of France) |
| DMSP | Defense Meteorological Satellite Program |
| DPC | Dipartimento Protezione Civile (of Italy) |
| EARS | EUMETSAT Advanced Retransmission Service |
| ECMWF | European Centre for Medium-range Weather Forecasts |
| EDC | EUMETSAT Data Centre, previously known as U-MARF |
| EUM | Short for EUMETSAT |
| EUMETCast | EUMETSAT's Broadcast System for Environmental Data |
| EUMETSAT | European Organisation for the Exploitation of Meteorological Satellites |
| FMI | Finnish Meteorological Institute |
| FTP | File Transfer Protocol |
| GEO | Geostationary Earth Orbit |
| GRAS-SAF | SAF on GRAS Meteorology |
| HDF | Hierarchical Data Format |
| HRV | High Resolution Visible (one SEVIRI channel) |
| H-SAF | SAF on Support to Operational Hydrology and Water Management |
| IDL© | Interactive Data Language |
| IFOV | Instantaneous Field Of View |
| IMWM | Institute of Meteorology and Water Management (in Poland) |
| IPF | Institut für Photogrammetrie und Fernerkundung (of TU-Wien, in Austria) |
| IPWG | International Precipitation Working Group |
| IR | Infra Red |
| IRM | Institut Royal Météorologique (of Belgium) (alternative of RMI) |
| ISAC | Istituto di Scienze dell'Atmosfera e del Clima (of CNR, Italy) |

| | |
|---|---|
| ITU | İstanbul Technical University (in Turkey) |
| LATMOS | Laboratoire Atmosphères, Milieux, Observations Spatiales (of CNRS, in France) |
| LEO | Low Earth Orbit |
| LSA-SAF | SAF on Land Surface Analysis |
| Météo France | National Meteorological Service of France |
| METU | Middle East Technical University (in Turkey) |
| MHS | Microwave Humidity Sounder (on NOAA 18 and 19, and on MetOp) |
| MSG | Meteosat Second Generation (Meteosat 8, 9, 10, 11) |
| MVIRI | Meteosat Visible and Infra Red Imager (on Meteosat up to 7) |
| MW | Micro Wave |
| NESDIS | National Environmental Satellite, Data and Information Services |
| NMA | National Meteorological Administration (of Romania) |
| NOAA | National Oceanic and Atmospheric Administration (Agency and satellite) |
| NWC-SAF | SAF in support to Nowcasting & Very Short Range Forecasting |
| NWP | Numerical Weather Prediction |
| NWP-SAF | SAF on Numerical Weather Prediction |
| O3M-SAF | SAF on Ozone and Atmospheric Chemistry Monitoring |
| OMSZ | Hungarian Meteorological Service |
| ORR | Operations Readiness Review |
| OSI-SAF | SAF on Ocean and Sea Ice |
| PDF | Probability Density Function |
| PEHRPP | Pilot Evaluation of High Resolution Precipitation Products |
| Pixel | Picture element |
| PMW | Passive Micro-Wave |
| PP | Project Plan |
| PR | Precipitation Radar (on TRMM) |
| PUM | Product User Manual |
| PVR | Product Validation Report |
| RMI | Royal Meteorological Institute (of Belgium) (alternative of IRM) |
| RR | Rain Rate |
| RU | Rapid Update |
| SAF | Satellite Application Facility |
| SEVIRI | Spinning Enhanced Visible and Infra-Red Imager (on Meteosat from 8 onwards) |
| SHMÚ | Slovak Hydro-Meteorological Institute |
| SSM/I | Special Sensor Microwave / Imager (on DMSP up to F-15) |
| SSMIS | Special Sensor Microwave Imager/Sounder (on DMSP starting with S-16) |
| SYKE | Suomen ympäristökeskus (Finnish Environment Institute) |
| $T_{BB}$ | Equivalent Blackbody Temperature (used for IR) |

| | |
|---|---|
| TKK | Teknillinen korkeakoulu (Helsinki University of Technology) |
| TMI | TRMM Microwave Imager (on TRMM) |
| TRMM | Tropical Rainfall Measuring Mission UKMO |
| TSMS | Turkish State Meteorological Service |
| TU-Wien | Technische Universität Wien (in Austria) |
| U-MARF | Unified Meteorological Archive and Retrieval Facility |
| UniFe | University of Ferrara (in Italy) |
| URD | User Requirements Document |
| UTC | Universal Coordinated Time |
| VIS | Visible |
| ZAMG | Zentralanstalt für Meteorologie und Geodynamik (of Austria) |